

RESEARCH ARTICLE

10.1002/2017JA023901

Traveling Foreshocks and Transient Foreshock Phenomena

Key Points:

- Different types of foreshocks exist
- Relations between different types of foreshocks and foreshock transient phenomena
- All foreshock phenomena are put in a single scheme in solar foreshock coordinates

Correspondence to:

P. Kajdič,
primoz@igeofisica.unam.mx

Citation:

Kajdič, P., Blanco-Cano, X., Omidi, N., Rojas-Castillo, D., Sibeck, D. G., & Billingham, L. (2017). Traveling foreshocks and transient foreshock phenomena. *Journal Geophysical Research: Space Physics*, 122, 9148–9168, <https://doi.org/10.1002/2017JA023901>

Received 20 JAN 2017

Accepted 22 AUG 2017

Accepted article online 28 AUG 2017

Published online 25 SEP 2017

P. Kajdič¹ , X. Blanco-Cano¹, N. Omidi² , D. Rojas-Castillo³ , D. G. Sibeck⁴ , and L. Billingham⁵ 

¹Instituto de Geofísica, Universidad Nacional Autónoma de México, Mexico City, Mexico, ²Solana Scientific Inc., Solana Beach, California, USA, ³Swedish Institute of Space Physics, Kiruna, Sweden, ⁴NASA GSFC, Greenbelt, Maryland, USA, ⁵British Geological Survey, Edinburgh, UK

Abstract We use the multispacecraft capabilities of the Cluster and Time History of Events and Macroscale Interactions during Substorms (THEMIS) missions to show that two types of foreshock may be detected in spacecraft data. One is the global foreshock that appears upstream of the Earth's quasi-parallel bow shock under steady or variable interplanetary magnetic field. Another type is a traveling foreshock that is bounded by two rotational discontinuities in the interplanetary magnetic field and propagates along the bow shock. Foreshock compressional boundaries are found at the edges of both types of foreshock. We show that isolated foreshock cavities are a subset of the traveling foreshocks that form when two bounding rotational discontinuities are so close that the ultralow-frequency waves do not develop in the region between them. We also report observations of a spontaneous hot flow anomaly inside a traveling foreshock. This means that other phenomena, such as foreshock cavitons, may also exist inside this type of foreshock. In the second part of this work we present statistical properties of phenomena related to the foreshock, namely, foreshock cavities, cavitons, spontaneous hot flow anomalies, and foreshock compressional boundaries. We show that spontaneous hot flow anomalies are the most depleted transient structures in terms of the B field and plasma density inside them and that the foreshock compressional boundaries and foreshock cavities are closely related structures.

Plain Language Summary Solar wind (SW) is ionized and magnetized gas propagating radially away from the Sun at supersonic speeds. When it encounters obstacles, such as our planet's magnetosphere, the SW is decelerated, deflected, and heated in a thin shock wave that stands in front of the obstacle. In case of Earth, its shock wave is supercritical, meaning that it reflects a portion of incoming SW particles (ions and electrons) that are reflected back sunward. If the conditions are right, these particles escape far upstream. The interaction of these reflected particles with the SW ones creates a region upstream of the Earth's bow shock called the foreshock region. In it the magnetic field is perturbed and different populations of ions inhabit it. Such region is called global foreshock of Earth. Here we describe another type of foreshock, which we call traveling foreshock, that occurs when the upstream interplanetary magnetic field (IMF) changes its orientation. This occurs since the IMF is composed of magnetic flux tubes that are not straight and are convected by the SW antisunward. In order to distinguish between the global and traveling foreshocks, multispacecraft observations are required. We discuss the relationships of different types of foreshocks with different foreshock phenomena.

1. Introduction

As the solar wind (SW) flows away from the Sun, it encounters obstacles, such as planets and their magnetospheres. Close to them, the SW is decelerated, deflected, and heated by the shock waves that stand in front of these obstacles. Due to their shapes, these shock waves are referred to as bow shocks. They are collisionless in nature because the mean free path of ions is much larger than the bow shock sizes.

The most studied bow shock is the one standing in front of our planet. On average, its subsolar point is located $\sim 13 R_E$ sunward of the Earth, but this distance can vary between $10 R_E$ and $20 R_E$ (e.g., Meziane et al., 2014). Its Alfvénic and magnetosonic Mach numbers (M_A and M_{ms} , respectively) typically range between $6 \leq M_A \leq 7$ and $5 \leq M_{ms} \leq 6$ (Winterhalter & Kivelson, 1988). Due to such high Mach numbers, the bow shock of Earth

is supercritical, meaning that it dissipates most of the SW kinetic energy by reflecting a portion of incident SW ions (e.g., Treuman, 2009, and references therein).

An important parameter that determines what is observed upstream of the Earth's bow shock in terms of waves and particles is the angle between the upstream interplanetary magnetic field (IMF) and the shock normal, θ_{BN} . Most of the foreshock phenomena are observed for $\theta_{BN} < 45^\circ$. Thus, we commonly refer to the portion of the bow shock with θ_{BN} less (more) than 45° as quasi-parallel (quasi-perpendicular) shock.

Observations, however, show backstreaming ions for $\theta_{BN} \leq 70^\circ$ (e.g., Eastwood et al., 2005). These ions exhibit relatively cold distributions and propagate upstream along the IMF; hence, they are called field-aligned ion beams (FABs) (Gosling et al., 1978, 1979; Thomsen, 1985; Kis et al., 2007; Meziane et al., 2013). Their energies tend to be $\lesssim 10$ keV. FABs interact with the incoming SW particles, and this can result in the growth of ultralow-frequency (ULF) waves (e.g., Gary, 1993; Dorfman et al., 2017) with typical periods of ~ 30 s. Since they need some time to grow, the ULF waves are not observed together with the FABs but rather together with the so-called intermediate ion distributions (Paschmann et al., 1979). Finally, as the ULF waves propagate through regions where suprathermal particles exhibit strong density gradients, they steepen and thus gain a significant compressive component. Such waves are observed together with diffuse ion populations (e.g., Fuselier et al., 1986; Kis et al., 2004; Eastwood et al., 2005). The diffuse and intermediate ions exhibit energies up to several hundreds of keV. FABs, intermediate, and diffuse ions are commonly called suprathermal ions. The region upstream of Earth's bow shock populated by ULF waves (suprathermal ions) is called the ULF wave (suprathermal ion) foreshock (e.g., Eastwood et al., 2005, and references therein).

The ULF waves propagate sunward in the SW frame of reference but are convected by the SW toward the bow shock. As ULF waves approach the bow shock, they steepen and can form shocklets (e.g., Hoppe & Russell, 1981, 1983; Hada & Kennel, 1987) and short-large-amplitude magnetic structures (SLAMS) (e.g., Thomsen et al., 1990; Schwartz & Burgess, 1991; Schwartz et al., 1992; Mann et al., 1994; Lucek et al., 2002). The interaction of compressive and transverse ULF waves leads to the formation of foreshock cavitons (Omidi, 2007; Blanco-Cano et al., 2009, 2011; Kajdić et al., 2011, 2013). Cavitons convected by the SW generate spontaneous hot flow anomalies (SHFAs) (Zhang et al., 2013; Omidi et al., 2013b, 2014) when they arrive to the bow shock.

Another structure commonly observed at the edges of the foreshock is the foreshock compressional boundary (FCB) (Omidi et al., 2009; Rojas-Castillo et al., 2013). These structures separate either the pristine solar wind or the region populated by field-aligned ion beams from the region of the foreshock populated by compressive ULF waves and diffuse ions.

FCBs have been associated with foreshock cavities (Schwartz et al., 2006; Billingham et al., 2008, 2011). While the earlier works referred to foreshock cavities as isolated structures, Billingham et al. (2011) talk about boundary cavities that are found at the edges of the foreshock and were later referred to as FCBs. Omidi et al. (2013a) performed global hybrid simulations of planetary bow shock, under varying upstream conditions. Specifically, the authors reproduced foreshock cavities by launching two consecutive IMF rotational discontinuities between which the IMF connected to the otherwise quasi-perpendicular bow shock in such a way that the local θ_{BN} was less than 45° . This leads to the development of foreshock-like regions upstream of a portion of the simulated bow shock between the two IMF discontinuities, which were convected along the bow shock surface. These regions were called by the authors foreshock cavities and also traveling foreshocks. FCBs formed at the edges of these regions.

In the first part of this work we use Time History of Events and Macroscale Interactions during Substorms (THEMIS) and Cluster multispacecraft observations to perform case studies of foreshocks and foreshock cavities to confirm some of the predictions made by Omidi et al. (2013a): we show that the spacecraft sometimes observe the global Earth's foreshock and sometimes a traveling foreshock. The global foreshock may be observed upstream of the quasi-parallel section of the Earth's bow shock under either steady or variable IMF conditions. When the IMF changes its orientation, the foreshock changes its location with respect to the bow shock. Two consecutive IMF rotations may cause the global foreshock to rock back and forth, resulting in a spacecraft initially located in the unperturbed solar wind to enter and then exit the foreshock.

We note here that traveling foreshocks should not be mistaken for another type of transient localized foreshocks that have recently been discovered by Pfau-Kempf et al. (2016), which occur due to bow shock perturbations caused by flux transfer events under stable solar wind and IMF conditions.

In a different scenario, an IMF flux tube is convected along the bow shock. The spacecraft observes two IMF rotational discontinuities (RDs) (Note that here we do not distinguish between rotational and tangential discontinuities.) During the time between the RDs, the geometry of a portion of the bow shock may change from quasi-perpendicular ($\theta_{BN} > 45^\circ$) to quasi-parallel ($\theta_{BN} < 45^\circ$), which leads to the formation of a region between the RDs that is populated by suprathermal particles and ULF fluctuations. As the two RDs propagate along the bow shock, so does the perturbed region between them. We call such a region a traveling foreshock.

The only way to observationally distinguish between the back and forth motion of the global foreshock and the traveling foreshock is by using simultaneous observations of several spacecraft. In the first case the spacecraft observe the arrival of the foreshock at slightly different times in a certain sequence. If the spacecraft spatial configuration does not change, then the sequence in which they exit the foreshock is reversed. Such signatures in the spacecraft data are known as nested signatures (e.g., Burgess, 2005). On the other hand the sequence in which the spacecraft observe the traveling foreshock is the same as the sequence in which they exit it. The so-called convected signatures (Burgess, 2005) can be found in the spacecraft data in this case.

In the second part of this work we statistically compare observational properties of foreshock cavities, foreshock cavitons, foreshock compressional boundaries, and spontaneous hot flow anomalies. We also compare their locations and the solar wind and IMF conditions under which they are observed.

This paper is organized as follows: in section 2.1 we present the instruments and data used in this study. In section 2.2 we show multispacecraft observations of the global foreshock, the traveling foreshocks, and foreshock cavities. In section 2.3 we exhibit statistics of observational properties of several types of transient foreshock phenomena. In section 3 we discuss the results, and in section 4 we summarize our findings.

2. Observations

2.1. Instruments and Data Sets

We use multispacecraft data provided by the Cluster and THEMIS missions.

The Cluster mission consists of four identical spacecraft that provide magnetic field and plasma measurements in the near-Earth environment. The spacecraft carry several instruments, including a Fluxgate Magnetometer (FGM) (Balogh et al., 2001) and the Cluster Ion Spectrometer (CIS) (Rème et al., 2001). We use FGM magnetic field vectors and CIS-HIA solar wind ion moments with 0.2 s and 4 s time resolution, respectively.

The THEMIS mission consists of five spacecraft. Their Fluxgate Magnetometer (Auster et al., 2008) measures the background magnetic field with time resolution up to 64 Hz. Here we use data with 0.25 s resolution. The THEMIS ion and electron analyzers (IESA and eESA) (McFadden et al., 2008) provide plasma moments and spectrograms with a spin (3 s) time resolution.

The data were accessed through the European Space Agency's Cluster Science Archive (<http://www.cosmos.esa.int/web/csa>) and through the CIWeb portal (<http://clweb.irap.omp.eu>) which is maintained by the Institut de Recherche en Astrophysique et Planétologie.

2.2. Case Studies

2.2.1. The Global Foreshock

This section presents THEMIS observations of the global foreshock. THEMIS A observed the foreshock on 7 August 2007 between 2:10 UT and 2:44 UT. Figure 1 shows the data between 01:51 UT and 03:03 UT on the same day. The following quantities are displayed in the panels from top to bottom: (a) magnetic field magnitude in units of nanotesla (nT), (b) magnetic field components in GSE coordinate system in units of nT, (c) angle between the IMF and the Sun-Earth line in degrees, (d) IMF clock angle in degrees, (e) SW density in cm^{-3} , (f) solar wind speed (black) and $-V_x$ component (red) in km s^{-1} , (g) V_y and V_z components of SW velocity in km s^{-1} , (h) SW temperature in eV, (i) ion spectra with colors representing the logarithm of the particle energy flux (units $\text{eV}/(\text{cm}^{-1} \text{ s sr eV})$), (j), Morlet wavelet spectrum for B magnitude, (k) Morlet wavelet spectrum for B_x component, and (l) B magnitude and B_x component between 02:25 and 02:30 UT.

We can see that from 01:51 UT to 02:09 UT the IMF was relatively steady with only small rotations. The θ_{BX} (which is similar to θ_{BN} near the Sun-Earth line) displayed values between 60° and 90° . During this time the THEMIS A spacecraft observed the pristine SW. At 02:09 UT (first vertical red line) the θ_{BX} starts diminishing until $\sim 02:16$ UT (second vertical red line) when it reached values below 20° . During this time interval the THEMIS A spacecraft entered the foreshock region. Several things point to the following: the spacecraft became immersed in strong B field fluctuations with amplitudes $\delta B/B$ up to 0.5 and periods of several tens

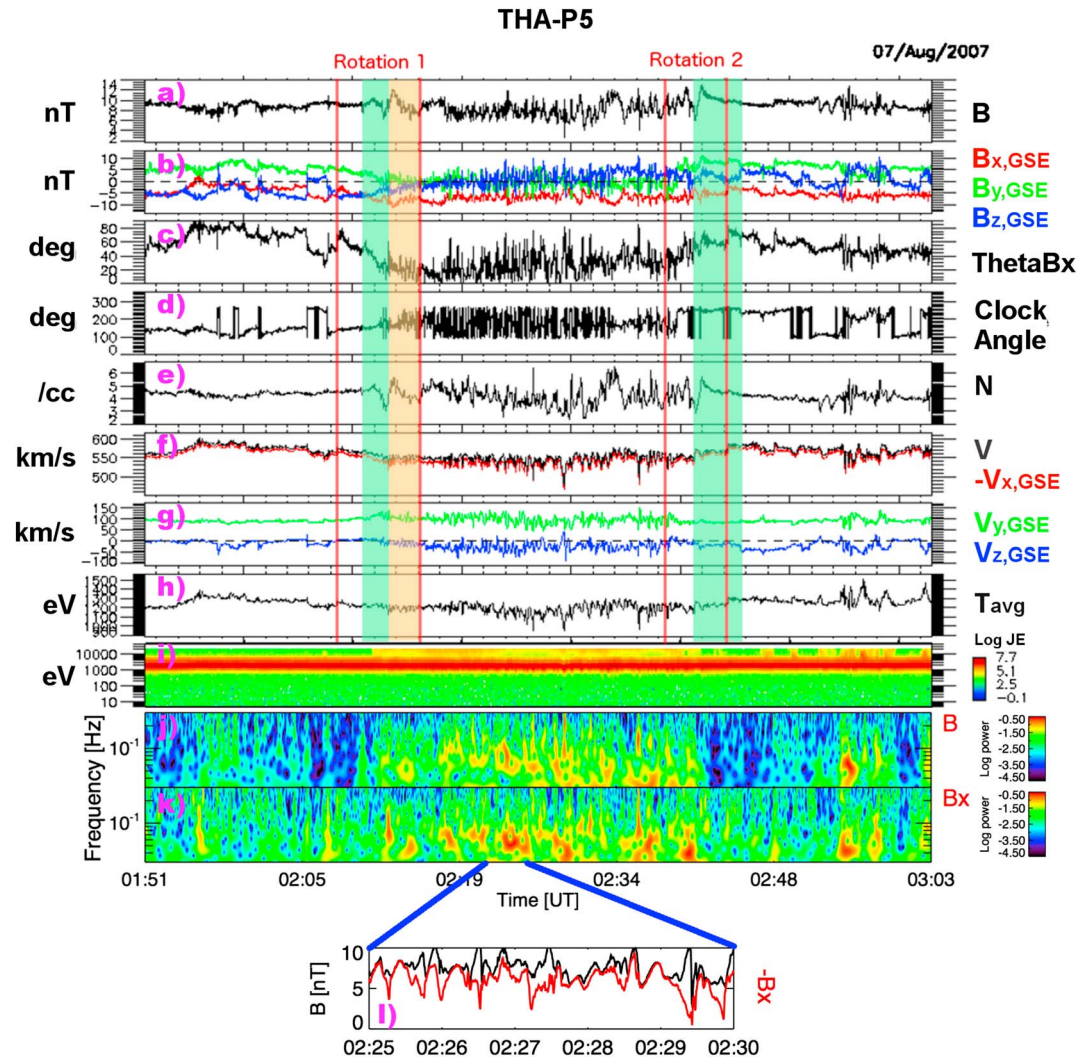


Figure 1. THEMIS A data between 01:51 UT and 03:03 UT on 7 August 2007. (a) Magnetic field magnitude in units of nanotesla (nT), (b) magnetic field components in GSE coordinate system in units of nT, (c) angle between the IMF and the Sun-Earth line in degrees, (d) IMF clock angle in degrees, (e) SW density in cm^{-3} , (f) solar wind speed (black) and $-V_x$ component (red) in km s^{-1} , (g) V_y and V_z components of SW velocity in km s^{-1} , (h) SW temperature in eV, (i) ion spectra with colors representing the logarithm of the particle energy flux (units $\text{eV}/(\text{cm}^{-1} \text{ s sr eV})$), (j) Morlet wavelet spectrum for B magnitude, (k) Morlet wavelet spectrum for B_x component, and (l) B magnitude and B_x component between 02:25 and 02:30 UT.

of seconds. These fluctuations contained a significant compressive component and are known as ULF waves. Intense fluctuations also appeared in the density and velocity panels. The bottom panel revealed the onset of suprathermal ion population (energies $\lesssim 30$ keV) starting at $\sim 02:12$ UT.

Inside this foreshock the IMF and plasma parameters change with respect to the upstream solar wind: the average B field magnitude decreases from ~ 8.5 nT to ~ 7.5 nT, the average plasma density from $\sim 4.3 \text{ cm}^{-3}$ to $\sim 3.8 \text{ cm}^{-3}$, and the average plasma velocity from $\sim 573 \text{ km s}^{-1}$ to $\sim 357 \text{ km s}^{-1}$. A detailed inspection of the ion spectrum in Figure 1 reveals that this decrease of plasma velocity is not due to the deceleration of the incident solar wind so it must be due to the contribution of suprathermal ions arriving from the Earth's bow shock to the total plasma bulk velocity. We know this since the energy of the peak of the SW beam does not change. The latter primarily diminishes due to the V_x component, while the absolute values of the V_z component increase slightly (from $\sim 82 \text{ km s}^{-1}$ to $\sim 102 \text{ km s}^{-1}$). At 02:38 UT (third vertical red line) the θ_{BX} starts to increase again until 02:44 UT (fourth vertical red line). After that time the θ_{BX} values stay above 50° and the plasma and IMF parameters are steady. The suprathermal ions disappear at 02:43 UT. The spacecraft stays in the

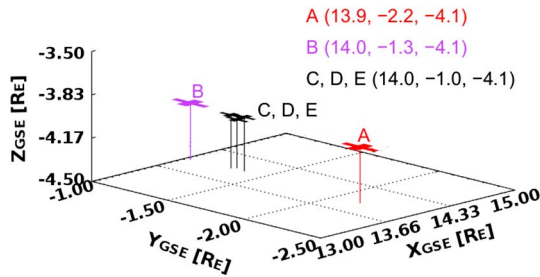


Figure 2. Spatial configuration of the five THEMIS spacecraft during the 7 August 2007 event.

SW for the next few minutes. Before the end of the shown time interval at 03:03 UT, the spacecraft detects the suprathermal ions and ULF compressive fluctuations several more times but for shorter time intervals.

The two regions shaded in green in Figure 1 mark the intervals when a foreshock compressional boundary (FCB) is detected. These phenomena (see, e.g., Rojas-Castillo et al., 2013) are commonly observed at the edges of the foreshock and are characterized by correlated increments in B and N above the upstream SW values, followed by a drop below the upstream SW values.

The first FCB is quite weak with only a small hump in B and N . The trailing FCB is much more prominent. The suprathermal ions appear and disappear just when the B and N inside the two FCBs reach their maximum values at 02:14 UT and 02:43 UT, respectively.

We examine the ULF wave properties more closely in Figures 1j and 1l. We can see that the ULF waves are compressive since both wavelet spectra exhibit similar power and since the B magnitude in Figure 1l shows irregular ULF fluctuations. The frequencies of these waves are between 2×10^{-1} Hz and 8×10^{-2} Hz corresponding to periods between ~ 10 s and 50 s.

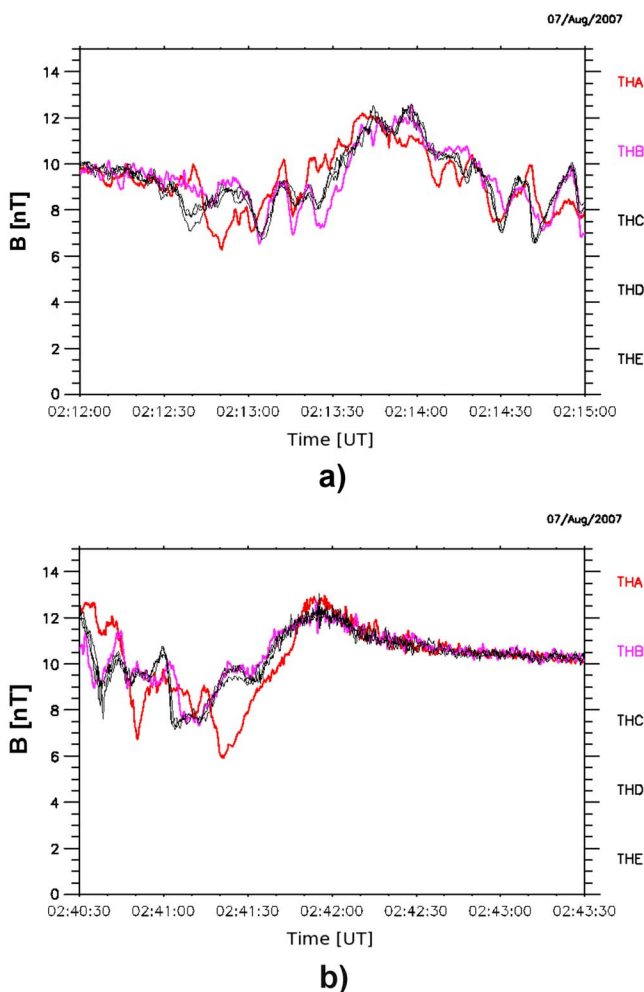


Figure 3. Magnetic field magnitude profiles of (a) the leading and (b) the trailing edges associated to the foreshock detected on 7 August 2007. Red line represents the THEMIS A data, purple line the THEMIS B data, while the data of the other three spacecraft are represented by the black traces.

In order to answer the question about which type of foreshock (global or traveling) THEMIS A observed, we perform a multispacecraft analysis of this event. As can be seen in Figure 2 the THEMIS spacecraft were in a string-of-pearls configuration along y_{GSE} direction. At the time of the event they were positioned fairly near the Sun-Earth line. The leading spacecraft along their orbits was THEMIS B and the trailing THEMIS A, with the C, D, and E spacecraft located close together between THEMIS A and THEMIS B. In Figures 3a and 3b we show a close-up of B field profiles of the leading and trailing parts of the foreshock interval presented in Figure 1. Since the leading FCB was weak, we examine a structure observed just after it. It is shaded in orange in Figure 1. The red trace in Figures 3a and 3b corresponds to THEMIS A, the purple to THEMIS B, while the thin black traces, which can hardly be distinguished from each other, correspond to the C, D, and E spacecraft. In Figure 3a we see that THEMIS A detected the structure first (starting at $\sim 02:13:18$ UT), while THEMIS B ($\sim 02:13:29$ UT) was the last to observe it. Spacecraft C, D, and E entered the structure roughly at 02:13:27 UT.

We can see in Figure 3b that the sequence in which the spacecraft observed the trailing FCB was reversed. THEMIS B detected this FCB starting at $\sim 02:41:15$ UT, slightly before the C, D, and E spacecraft ($\sim 02:41:17$ UT), while THEMIS A was the last to detect it $\sim 02:41:24$ UT. The B, C, D, and E spacecraft observed a more extended FCB than the A spacecraft. This is probably because (1) each spacecraft crossed the structure at slightly different place and (2) they detected it at slightly different times during which the FCB could have evolved.

Figure 4 illustrates the situation in near-Earth interplanetary space around the times of arrival of the first (Figure 4a) and the second (Figure 4b) IMF rotation. Fairfield (1971) models for bow shock and magnetopause have been used here. In the figure the X_{GSE} axis points up, while the Y_{GSE} axis points right. In Figure 4a we see that the initial IMF orientation is such that the foreshock is located on the left side of the figure. At the first IMF rotation the foreshock becomes distorted, since the backstreaming ions follow the IMF lines that are connected to the bow shock surface in such a way that they make a small angle with its normal (nominally $\theta_{BN} < 45^\circ$). Upstream of the first rotation, the IMF is more radial and the foreshock shifts in the positive Y_{GSE} direction. This means that at some point during the rotation spacecraft will enter the foreshock region and it will observe a FCB. Once the rotation reaches the

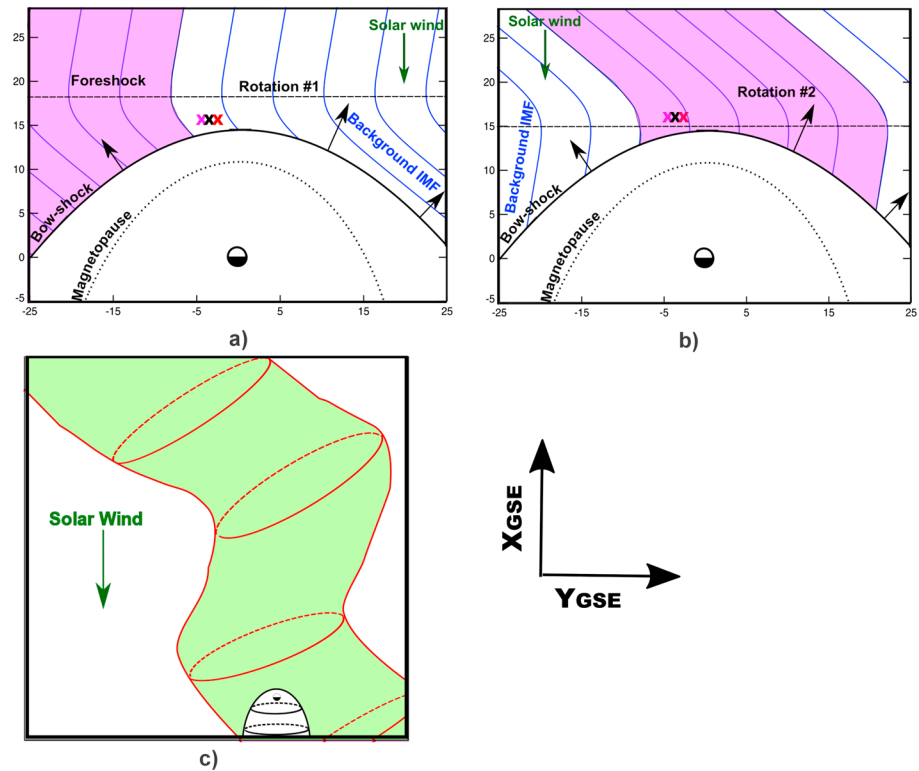


Figure 4. (a and b) Sketch of interplanetary magnetic field and foreshock configurations just before the interaction of two IMF rotations with the Earth's bow shock. Fairfield (1971) models for bow shock and magnetopause have been used here. The black arrows represent the local directions of the bow shock normal. The crosses represent spacecraft in a configuration similar to that in Figure 2. (c) A large wiggled magnetic flux tube passing by the bow shock would cause the observer to detect slowly rotating IMF and the nonconvecting (back and forth) motion of the foreshock as the θ_{BN} at every point on the bow shock surface changes with time. It should be stressed out that what is shown is just one scenario since in reality the properties of the flux tube, such as its extension, width, and spatial location, can be very different from the ones shown here.

bow shock, we have an almost radial foreshock. After some time a second IMF rotation arrives (Figure 4b). Upstream of this rotation the θ_{Bx} angle increases again, which causes the foreshock to move back toward the left side of the figure. Once this IMF rotation sweeps across the spacecraft and reaches the bow shock, the foreshock will be located the same way as it was before the arrival of the first IMF rotation. The spacecraft will move out of the foreshock and it will again observe a FCB.

2.2.2. The Traveling Foreshock

Our next case study occurred on 14 August 2007 between 20:56 UT and 21:13 UT (Figure 5). The five THEMIS spacecraft were in a configuration similar to that in the previous case (see Figure 6). Figure 5a presents the foreshock region similar to that in the previous case, but now it is bounded by two IMF rotations both of which occur on much shorter time scales (a few seconds) than the rotations in the previous case study (~ 7 min); hence, we will call them rotational discontinuities (RDs). They are marked with vertical red lines. Before the first RD the angle between the IMF and the Sun-Earth line (θ_{Bx}) was $\sim 70^\circ$, and after the second RD it was above 80° . During the time between the two RDs B_x oscillated between 0° and 90° with an average value around $\sim 40^\circ$. As before, the two intervals shadowed in green mark the leading and trailing FCBs. We call the region between the two rotational discontinuities traveling foreshock for reasons that will become clear later. This region is populated by compressive ULF fluctuations and suprathermal ions.

Figure 7a shows B field magnitude profiles for the leading (Figure 7a) and the trailing (Figure 7b) FCBs. In Figure 7a we see that after about 2 min of steady B field with magnitude of ~ 5 nT observed by all spacecraft at slightly different times, the first to detect the leading FCB is THEMIS B (starting at $\sim 20:55:15$ UT), followed by C, D, and E ($\sim 20:55:19$ UT) spacecraft and THEMIS A is the last to detect it ($\sim 20:55:35$ UT). The detection times are marked with vertical lines in the figure. The same order is observed at the exit from the traveling foreshock, as it can be seen in Figure 7b. The fact that the order in which the spacecraft observed this foreshock is the

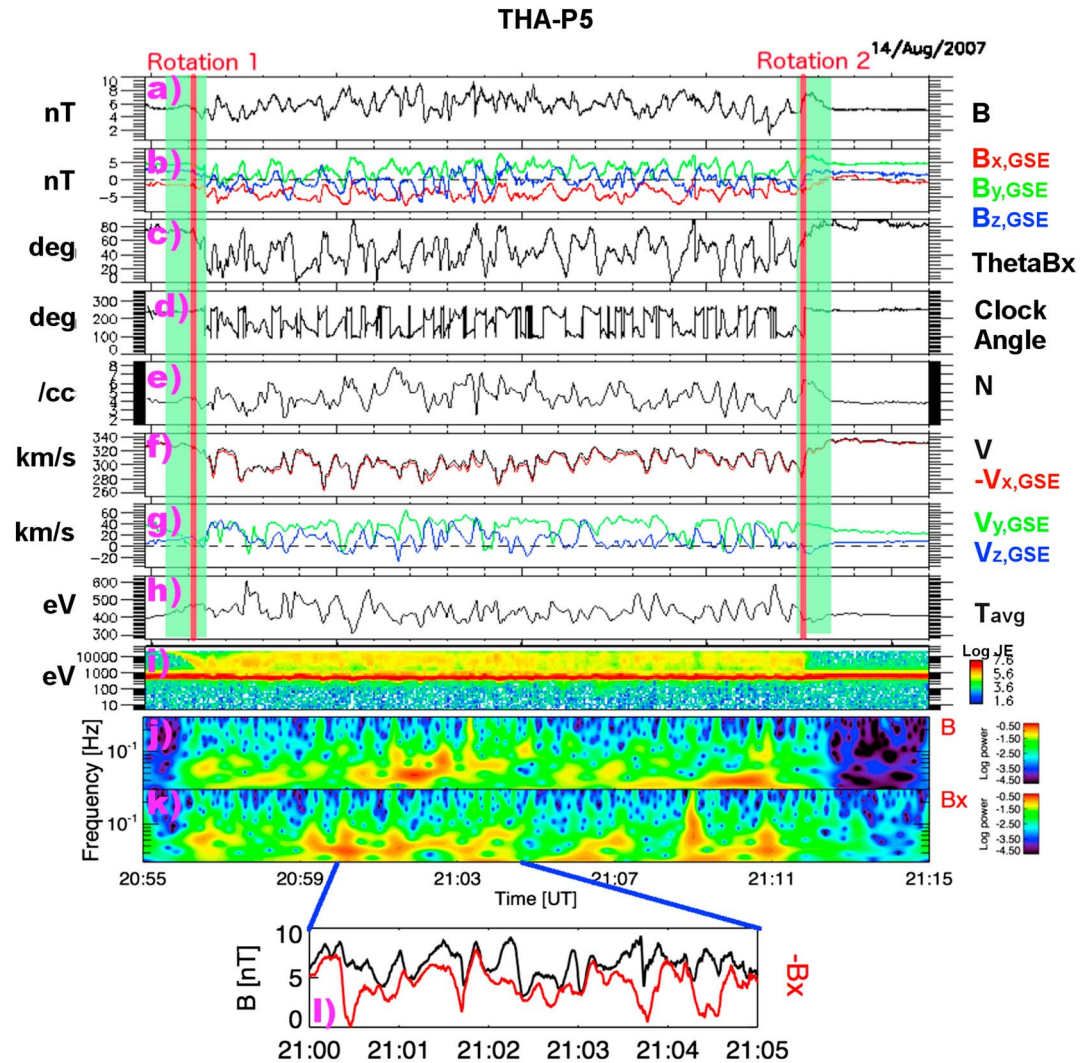


Figure 5. (a) THEMIS A data between 20:55 UT and 21:16 UT on 14 August 2007. The figure is in the same format as Figure 1. The two vertical red lines show two IMF RDs, and the intervals shadowed in green mark the FCBs at the edges of the traveling foreshock.

same when they enter and when they exit it tells us that this foreshock swept across the spacecraft; hence, we call it a traveling foreshock.

Figure 8a illustrates the situation in this case. Again, Fairfield (1971) models for bow shock and magnetopause have been used here. The purple represents the global foreshock and the red a flux tube with different orientation than the background IMF (blue lines). The black arrows show the orientation of the local bow shock normal. The purple, black, and red crosses represent spacecraft in a configuration similar to that in Figure 6. The magnetic flux tubes are carried anti-sunward (downward in the figure) by the solar wind. Therefore, the intersection of the red flux tube with the bow shock propagates along the Y_{GSE} direction. The traveling foreshock also propagates in the same direction (indicated by the red arrow). The local bow shock geometry changes to quasi-parallel at places where the tube's field lines connect to the bow shock, so a foreshock region forms upstream of this portion of the bow shock. This is a traveling foreshock that propagates along the Y_{GSE} axis due to the way in which B field lines in it are oriented. Note that in this figure the width of the flux tube is smaller than the width of the bow shock, while in reality it can be larger.

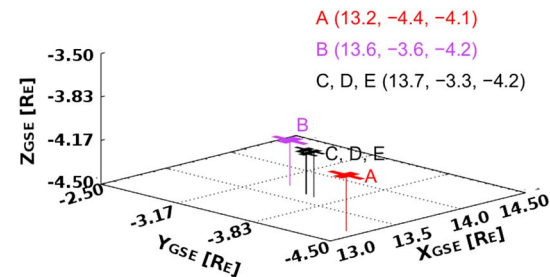


Figure 6. Spatial configuration of the five THEMIS spacecraft during the 14 August 2007 observations of the traveling foreshock.

We calculate the average orientation of the magnetic field inside the traveling foreshock (hence the orientation of the flux tube) in GSE coordinates to be $(-0.59, 0.82, -0.20)$,

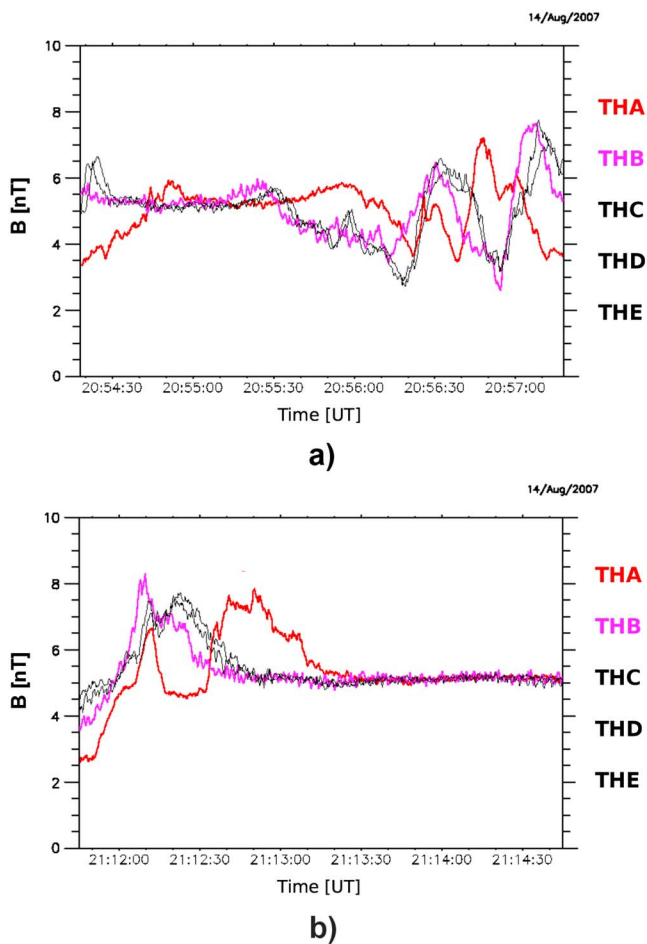


Figure 7. Magnetic field magnitude profiles of the (a) leading and (b) trailing edges of the foreshock detected on 14 August 2007. Red trace represents the THEMIS A data, purple trace the THEMIS B data, while the data of the other three spacecraft are represented by the black traces. Vertical lines mark times of the FCB peak, stated in the text.

but we can still see that this is a convected structure since the order in which the spacecraft entered is the same as the order in which they exited it.

These two events share some similarities with traveling foreshocks: inside both of them we observe suprathermal ions, they are convected structures, both are delimited by IMF RDs, and in the case of the longer-lasting cavity observed on 14 August 2007 there are even compressive ULF fluctuations inside it. The difference between the two cases shown here and the traveling foreshock shown in section 2.2.2 is that in the case of isolated cavities only a few or no ULF wave forms appear between the bounding IMF RDs, while in case of the traveling foreshock many compressive waves can be seen in the magnetic field and plasma data. Hence, we conclude that the events that are commonly called foreshock cavities are a subset of traveling foreshocks.

2.2.4. SHFA in a Traveling Foreshock

Our last case study is shown in Figure 11. It was observed on 9 August 2007 between 19:42:30 UT and 19:53 UT by the THEMIS spacecraft. The detailed inspection of multispacecraft observations reveals that this is a traveling foreshock which is bounded by two B field rotations, marked by two vertical red lines in Figure 11. The first rotation was particularly strong, and it marks the onset of field-aligned suprathermal ions with energies up to ~ 9 keV, which can be seen on the bottom panel. The magnetic field and density perturbations are small until about 19:48 UT. After that time there are compressive ULF fluctuations with $\delta B/B \sim 0.5$ and the intensity of the suprathermal ions increases. The energy range of these ions extends to much higher energies indicating a diffuse population. At 19:53:04 UT there is a less prominent B field rotation after which the suprathermal ions are still present although their intensity is much smaller and the B field and density perturbations

while the solar wind velocity in it was $\sim 310 \text{ km s}^{-1}$, predominantly in the negative X_{GSE} direction. The event lasted for 17 min in the spacecraft data. From this we can estimate the width of the flux tube to be $2.55 \cdot 10^5 \text{ km}$ or about $40 R_E$.

In Figure 5 we show the wavelet spectra of B (Figure 5j) and B_x (Figure 5k) and a 5 min zoom on the B and $-B_x$ (Figure 5l). Again, we see that the ULF waveforms are highly irregular and that they exhibit a strong compressible component.

In the next section we show that the mechanism that is responsible for the formation of traveling foreshocks is basically the same as the mechanism for the formation of another structure, called isolated foreshock cavities (Schwartz et al., 2006; Billingham et al., 2008). We suggest that isolated foreshock cavities can be considered a subset of traveling foreshocks.

2.2.3. Foreshock Cavities

This section presents two foreshock cavities. The first (Figure 9) was observed by the Cluster quartet on 28 December 2005. The event was first described by Billingham et al. (2008). It lasted for about a minute between 14:14 UT and 14:15 UT. It is bounded by two IMF RDs that are marked by red vertical lines. On the bottom panel we see that suprathermal ions are present during the time between the two IMF RDs. In Figure 9b we show B field magnitude profiles of the four spacecraft between 14:13 UT and 14:16 UT. The black, blue, green, and red are for C1, C2, C3, and C4 spacecraft, respectively. The spacecraft entered into this cavity in the following sequence, C2, C1, C4, and C3, and they exited it in the same order. This means that the cavity was convected past them. In this case the bounding rotations are close together and ULF waves are not observed between them.

Another foreshock cavity was observed on 14 August 2007 between 20:32 UT and 20:36 UT by the THEMIS B spacecraft (Figure 10a). This event is somewhat different from the previous case in the sense that the two IMF RDs (red vertical lines) are more separated and there are few ULF fluctuations that appear between them. Still, we classify this case study as a foreshock cavity as it resembles those published in the literature (see, for example, Figure 3 of Sibeck et al., 2002).

The B field magnitude data of the five THEMIS spacecraft are exhibited in Figure 10b. The signature of the structure is different in the THEMIS A data,

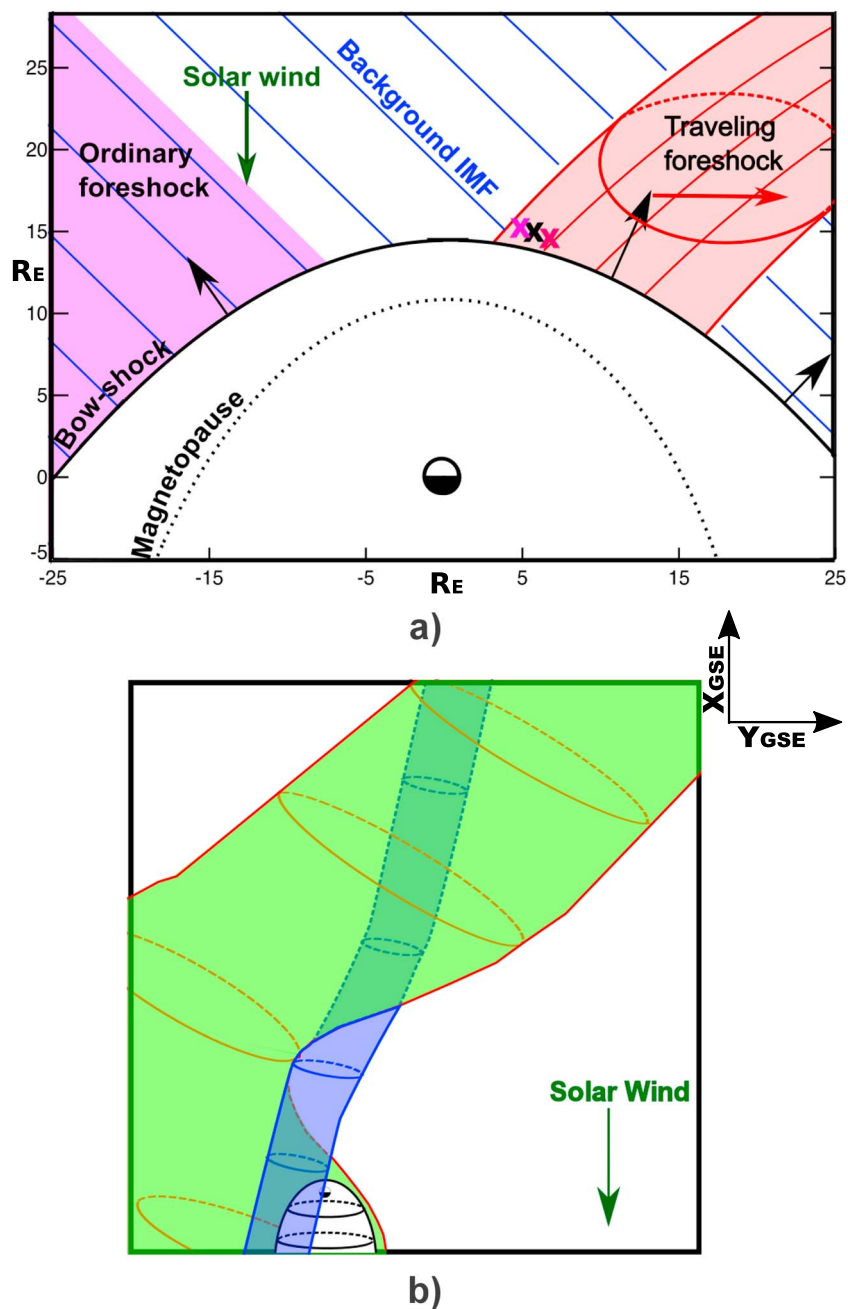


Figure 8. (a) Sketch of the event observed on 14 August 2007 (Fairfield (1971) models for bow shock and magnetopause have been used here). The purple represents the global foreshock, and the blue lines represent the IMF. The flux tube with different orientation than the background IMF is in red. The black arrows are the local bow shock normals. The red arrow determines the propagation of the traveling foreshock, while the green arrow shows the SW propagation direction. The crosses represent spacecraft in a configuration similar to that in Figure 6. (b) Due to twisted and braided magnetic field lines, the Earth's bow shock passes through different magnetic flux tubes. Here the bow shock is first inside the red flux tube; then it passes through a blue tube and returns into the red one. This results in rapid changes in the IMF orientation. As spacecraft cross an interface between two flux tubes, they observe a rotational discontinuity. Due to different IMF orientations inside the flux tube, spacecraft observe the convected foreshock signature.

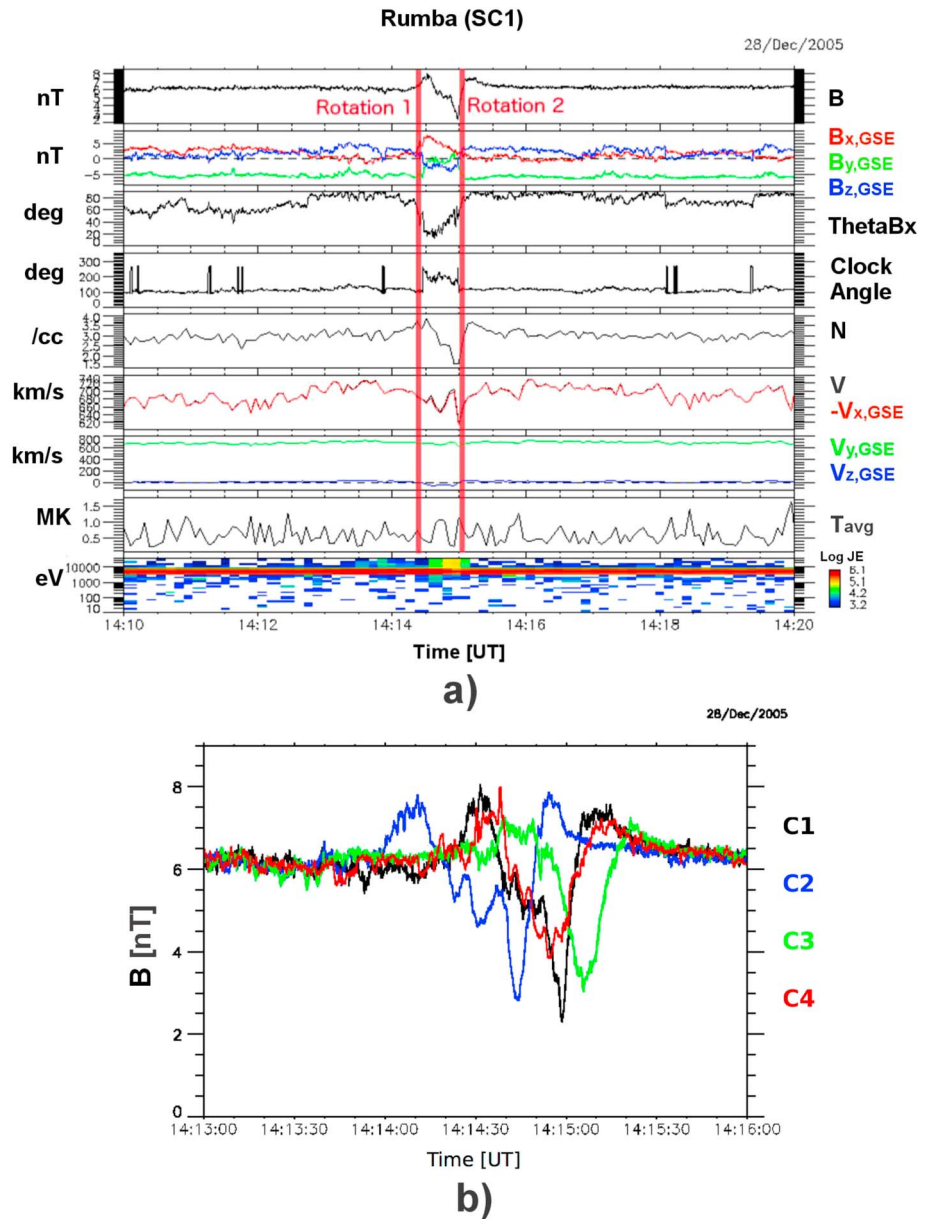
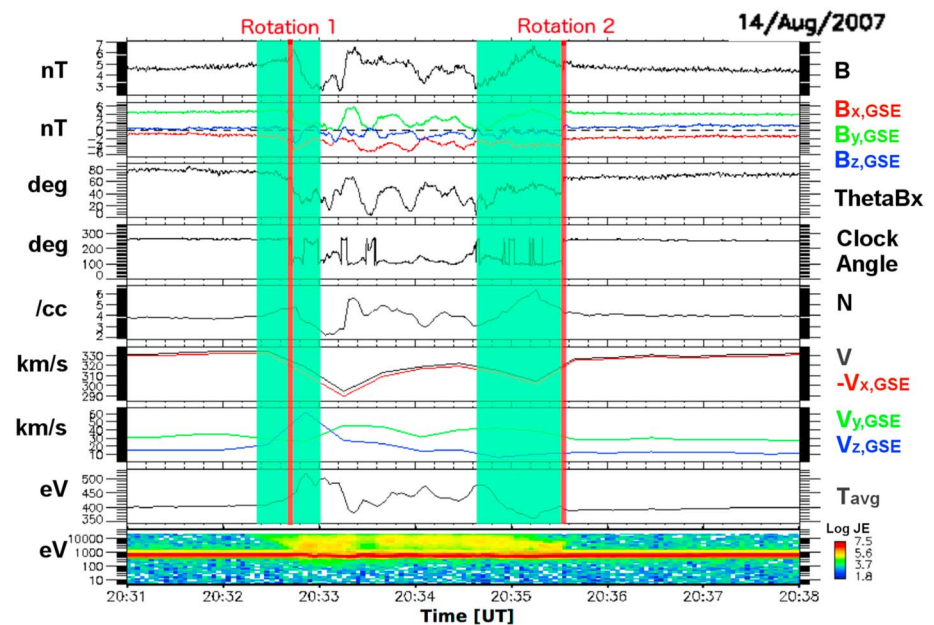


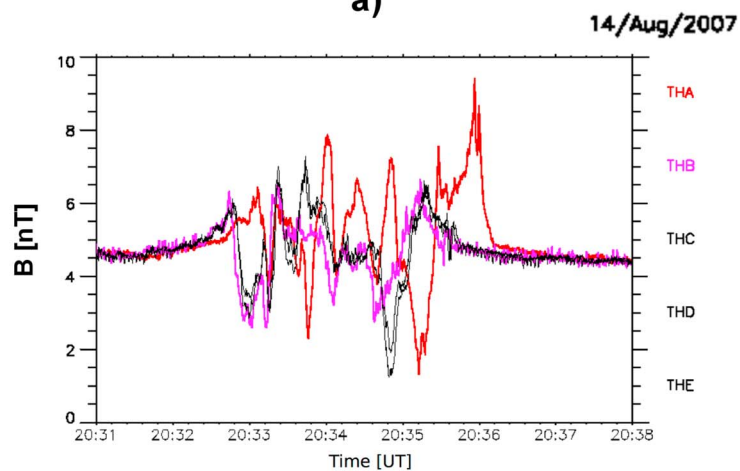
Figure 9. Foreshock cavity. (a) Cluster 1 data showing between 14:10 UT and 14:20 UT on 28 December 2005. The figure is in the same format as Figure 1 except that the temperature is in units of megakelvins (MK) and we do not show any wavelet spectra. (b) Magnetic field magnitude profiles of the four Cluster spacecraft during the 28 December 2005 event. The C1, C2, C3, and C4 data are represented by the black, blue, green, and red traces, respectively.

disappear. The spacecraft again entered the region of the foreshock populated by the field-aligned ion beams (e.g., Eastwood et al., 2005). At this time there is also a FCB.

An interesting feature appearing on this figure is a spontaneous hot flow anomaly (SHFA) centered at 19:50:58 UT (shaded in green in Figure 11). The SHFA exhibits typical signatures: B and N diminish at its center, but they are enhanced on its rims. There is an obvious increase of the proton temperature at the center (from 730 eV to 1340 eV). The absolute value of the x component of the plasma velocity decreases from 339 km s^{-1} to 192 km s^{-1} , the z component changes from -65 km s^{-1} to -264 km s^{-1} , and the total plasma velocity diminishes from 334 km s^{-1} to 241 km s^{-1} . This feature is not associated with a tangential IMF discontinuity; hence, we classify it as a spontaneous HFA, following the work of Zhang et al. (2013) and Omidi et al. (2013b, 2014). According to these authors, the SHFAs occur when foreshock cavitons (see Omidi, 2007; Blanco-Cano et al., 2009, 2011; Kajdič et al., 2011, 2013) interact with the Earth's bow shock. This case study



a)



b)

Figure 10. Foreshock cavity. (a) THEMIS A data between 20:31 UT and 20:38 UT on 14 August 2007. The figure is in the same format as Figure 9a). The vertical red lines mark the IMF RDs, and the intervals shadowed in green mark the FCBs. (b) Magnetic field magnitude profiles of the five THEMIS spacecraft during the 14 August 2007 intermediate event. Red line represents the THEMIS A data, purple line the THEMIS B data, while the data of the other three spacecraft are represented by the black traces.

tells us that the foreshock transient structures, such as foreshock cavities and SHFA, can form inside traveling foreshocks.

2.3. Statistical Comparison of Observational Properties of Upstream Phenomena

In the previous section we made several claims. For example, we pointed toward the relation between traveling foreshocks, FCBs, and foreshock cavities. We also showed that transient phenomena, such as SHFAs, can occur inside the traveling foreshocks. In this section we further strengthen our case by making use of statistical properties of these phenomena, namely, isolated foreshock cavities, foreshock cavities, spontaneous hot flow anomalies, and foreshock compressional boundaries. The data for all phenomena except SHFAs were compiled from the already existing literature. The cavity statistics were published by Billingham et al. (2008) (over 200 events), caviton properties by Kajdič et al. (2013) (92 events), and those for the FCBs by Rojas-Castillo et al. (2013) (36 events). To this, we add statistics of 19 SHFAs found in the Cluster data between the years 2003 and 2011 (listed in Table 1).

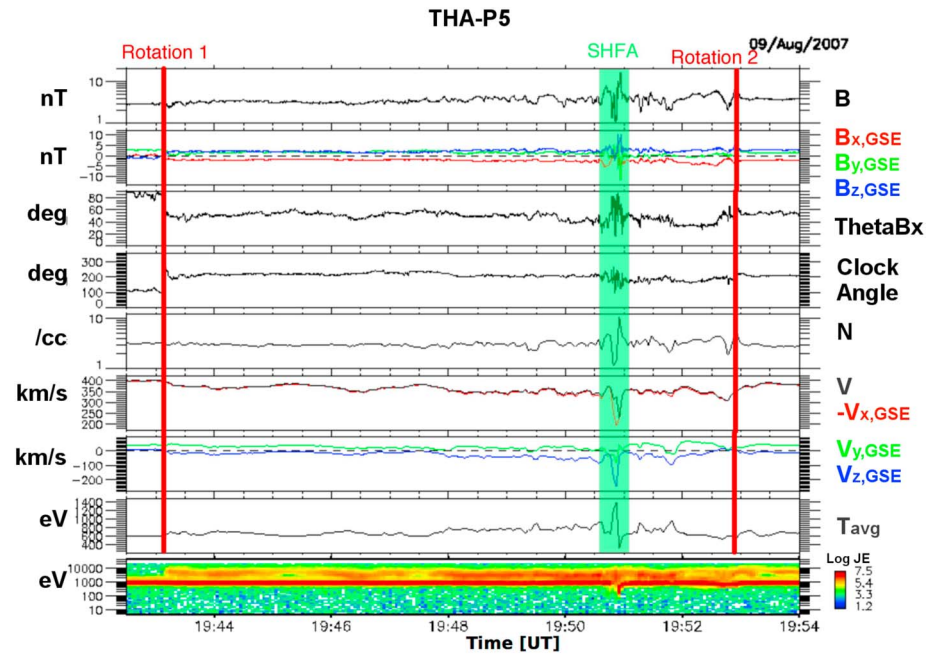


Figure 11. THEMIS A data between 19:42:30 UT and 19:54 UT on 9 August 2007. The figure is in the same format as Figure 9a except that B magnitude and plasma density N are represented on a logarithmic scale in order to bring out the compressive ULF waves in the traveling foreshock. The two vertical red lines show two IMF RDs delimiting the traveling foreshock, while the intervals shadowed in green show the spontaneous hot flow anomaly.

Histograms in Figure 12 show relative changes in the (from left to right) magnetic field magnitude, plasma density and velocity, and durations of (from top to bottom) SHFAs, foreshock cavitons, foreshock cavities, and FCBs. Δ sign marks the difference between the ambient SW value and the minimum value inside the structure (see Kajdič et al., 2013; Rojas-Castillo et al., 2013; Billingham et al., 2008, for details). In the case of FCBs it represents the difference between the maximum value inside the FCB and the upstream SW value. The upstream values were obtained by averaging the quantities during intervals adjacent to the events. The lengths of these intervals were typically of several tens of seconds up to a few minutes, although the exact lengths are different for each event. We can see that SHFAs are by far the most depleted structures with average $\Delta B/B$ and $\Delta N/N$ values of 0.9. In the case of the other three phenomena the average values of $\Delta B/B$ and $\Delta N/N$ are 0.5 for cavitons, 0.4 for cavities, and 0.4 for FCBs and the spread in values is much larger. The velocity does not change inside the cavitons (which is one of the criteria to identify them); it changes slightly in the case of foreshock cavities and across FCBs, while the change is significant in the case of SHFAs. The average durations of cavitons and SHFAs are similar (about 1 min), while they are longer (~ 107 s) in the case of foreshock cavities. All the described events last less than 200 s in the spacecraft data.

Figure 13 shows a scatterplot of $\Delta N/N$ versus $\Delta B/B$ for the four phenomena. We can see that in the case of FCBs (purple crosses) and foreshock cavitons (black asterisks) the two quantities are well correlated with correlation coefficients of 0.86 and 0.85, respectively. The correlation is less strong in the case of foreshock cavities (red diamonds, $k = 0.63$) and SHFAs (blue squares, $k = 0.30$). We can see again that the SHFAs cluster at highest values and are hence the most depleted structures.

Next we look at locations of these phenomena in solar foreshock coordinates (SFCs, Figure 15). These coordinates were first introduced by Greenstadt and Baum (1986) in their study of the location of the ULF compressional waves in the Earth's foreshock. Meziane and d'Uston (1998) used these coordinates to describe the observed locations of the intermediate ion boundary. Billingham et al. (2008) used them for foreshock cavities, while Kajdič et al. (2013) compared solar foreshock coordinates of foreshock cavitons to

Table 1

List of Spontaneous Hot Flow Anomalies

Date yyy-mm-dd	Start time [UT] hh:mm:ss	End time [UT] hh:mm:ss
2003-03-10	21:28:46	21:29:09
2003-04-12	00:22:56	00:23:52
2003-04-27	17:44:48	17:45:20
2003-04-30	03:41:35	03:42:27
2003-04-30	19:38:27	19:39:17
2006-03-10	15:30:26	15:31:05
2006-03-21	08:48:52	08:49:13
2006-05-23	01:58:49	01:58:58
2008-03-14	11:43:25	11:45:32
2008-04-07	02:57:22	02:58:15
2008-04-08	20:27:39	20:28:23
2009-03-19	14:37:09	14:38:20
2009-03-19	14:39:36	14:41:25
2009-03-30	12:39:32	12:41:44
2009-04-07	14:16:15	14:16:25
2009-04-23	04:47:38	04:48:40
2009-05-08	14:23:19	14:23:51
2011-02-07	10:13:10	10:14:20
2011-03-05	11:36:01	11:38:01

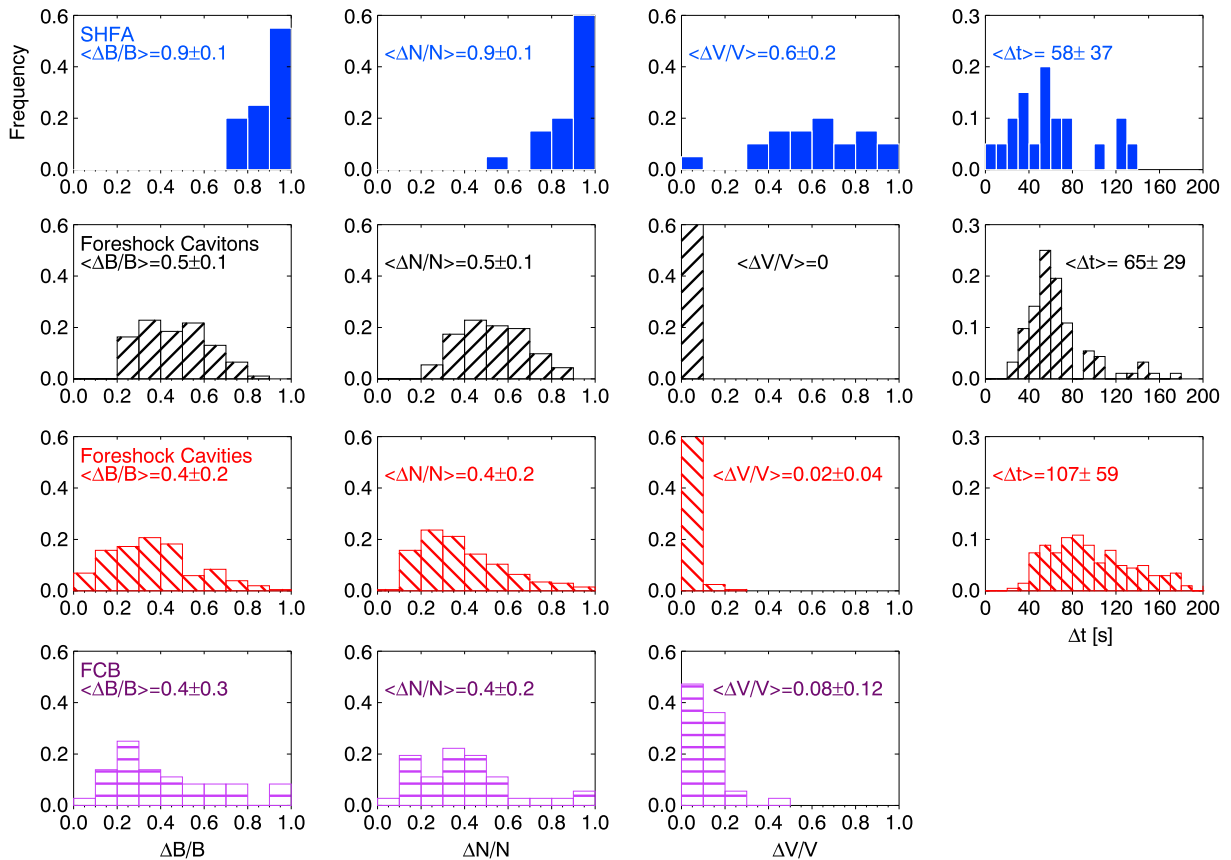


Figure 12. Some statistical distributions of observational properties of (first row) SHFAs, (second row) foreshock cavities, (third row) foreshock cavities, and (fourth row) FCBs. The following quantities are shown: relative changes of (from left to right) magnetic field magnitude, density, and plasma velocity and durations. The Δ sign marks the difference between the ambient SW value and the minimum value inside the structures. In case of FCBs it represents the difference between the maximum value inside the FCB and the upstream SW value.

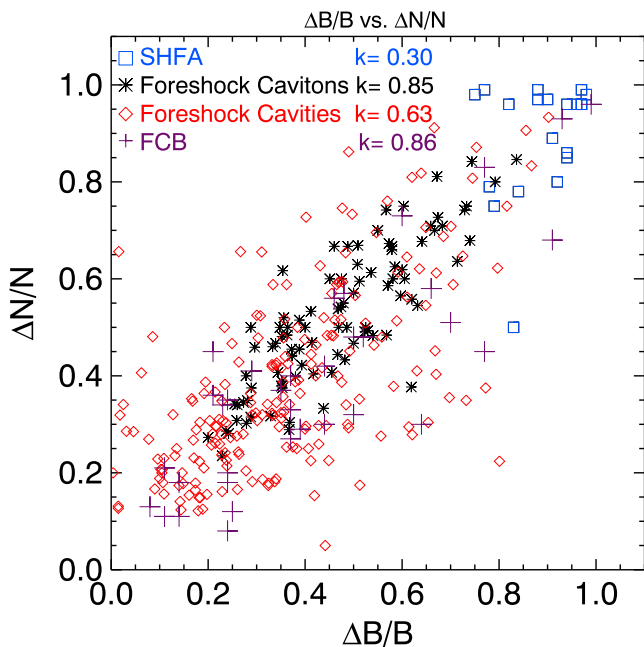


Figure 13. Scatterplot of $\Delta N/N$ versus $\Delta B/B$ for the four types of upstream transient phenomena.

those of intermediate ions and ULF waves. In order to calculate SFC, we must first determine the cross section of a model bow shock with a plane defined by the x axis and IMF direction. On this plane we define a set of rectangular coordinates (x, η) . The SFC consists of another set of coordinates (X_f, D_{BT}) . X_f is parallel to the Sun-Earth line and measures the distance between the observed structure and the tangential IMF line. D_{BT} measures the distance along this line between its intersection with the bow shock and the point with the same η coordinate as the observed structure.

To calculate SFC of our events, we model the bow shock shape as a hyperboloid and we use the solar wind dynamic pressure in order to scale the shock. We do this by first measuring solar wind properties during time intervals when the spacecraft were in the solar wind but were close to times when the structures (cavities, etc.) were observed. We then calculate the dynamic pressure and follow the procedure described in Jelínek et al. (2012) in order to obtain the stand-off distances of the bow shock. Next we calculate the ratio between each calculated stand-off distance and the stand-off distance of the nominal bow shock model used by Greenstadt et al. (1972) and Greenstadt and Baum (1986). The coordinates are calculated as explained in Greenstadt and Baum (1986).

The locations of the structures in SFC coordinates are presented in Figure 14a. In this figure the horizontal green line represents the tangent line. The dashed blue line is a fit to the ULF wave boundary by Greenstadt and Baum (1986),

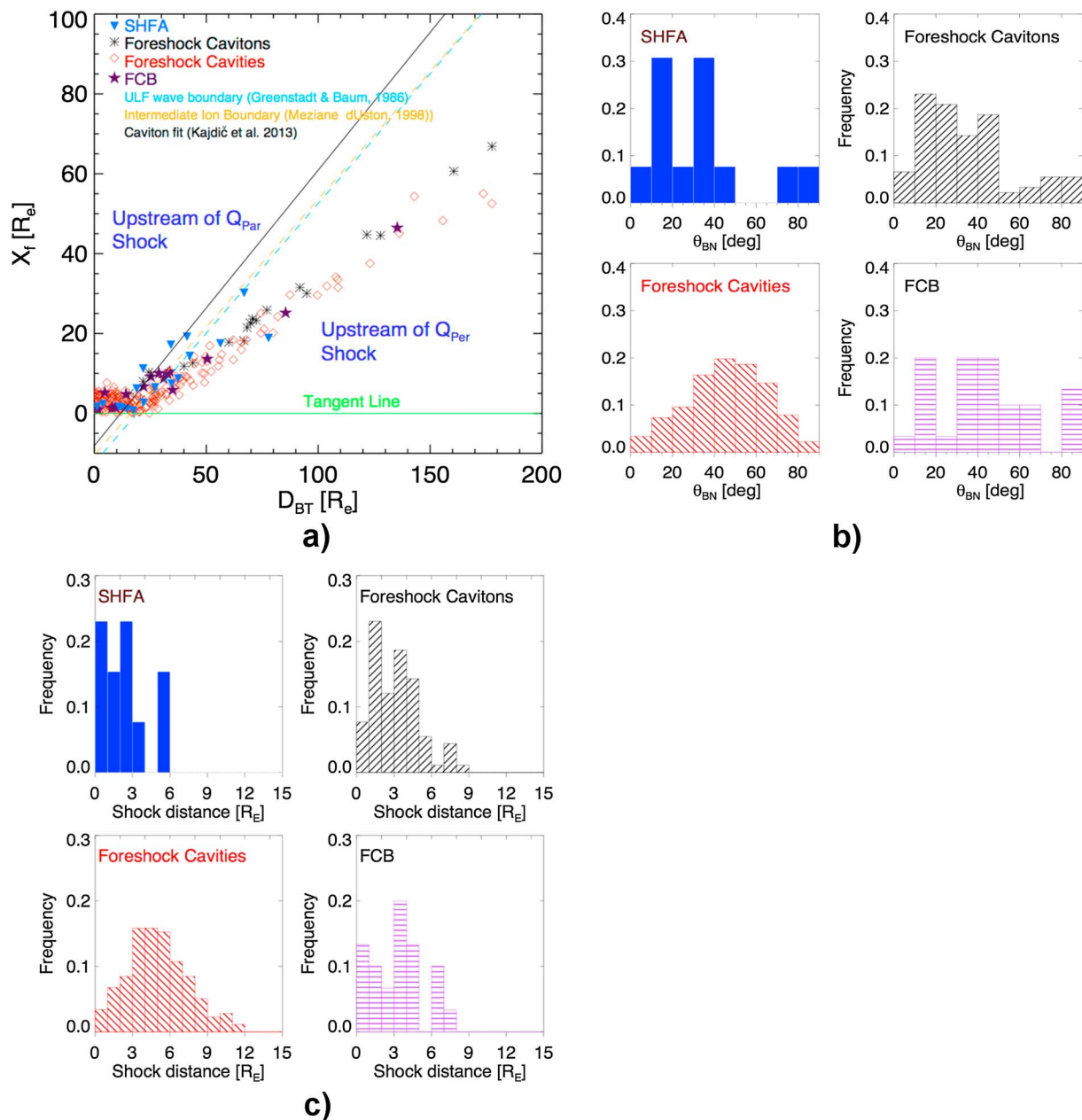


Figure 14. (a) Solar foreshock coordinates of the observed events. Black asterisks represent locations of foreshock cavities, blue triangles those of the SHFAs, red diamonds of the foreshock cavities, and purple stars of the FCBs. The horizontal green line represents a nominal tangent line. The dashed blue line is a fit to the ULF wave boundary by Greenstadt and Baum (1986), while the yellow dashed line represents a fit to ion intermediate boundary from Meziane and d’Uston (1998). The black continuous line is a fit to cavition locations from Kajdić et al. (2013). (b) Distributions of the angles θ_{BN} of the portions of the bow shock which different phenomena were magnetically connected to. (c) Distance (along the X_{GSE} axis) of the events to the model bow shock.

while the yellow dashed line represents a fit to ion intermediate boundary from Meziane and d’Uston (1998). The black continuous line is a fit to cavition locations from Kajdić et al. (2013). Black asterisks represent locations of foreshock cavities, blue triangles of the SHFAs, red diamonds of the foreshock cavities, and purple stars of the FCBs.

Kajdić et al. (2013), Billingham et al. (2008), and Meziane and d’Uston (1998) all used a single bow shock model for all their events. It can be seen in the figure that the locations of the structures (for example, foreshock cavities) calculated by us are very different from those in the past literature. Our approach with the bow shock scaled with the solar wind dynamic pressure is more accurate. One example to sustain this claim is

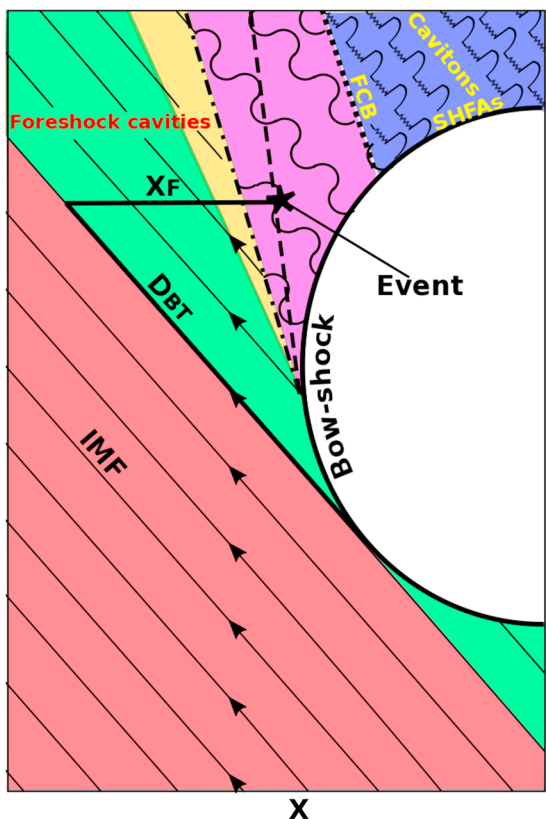


Figure 15. Solar foreshock coordinates and different boundaries and regions upstream of the bow shock. See text for details.

that in Figure 14a there are no events outside the tangent line, i.e., in the solar wind that is not magnetically connected to the bow shock, while this was the case when a single bow shock model was used.

The first phenomena observed downstream of the tangent line are foreshock cavities (red diamonds). Foreshock cavitons (black asterisks) lie farther downstream as expected, since the cavitons are always surrounded by compressive ULF waves. FCBs (purple stars) occupy the same region as cavities. This is because FCBs can appear at the edges of the traveling foreshocks and these are related to cavitites. Finally, SHFAs (blue triangles) tend to be found downstream of the cavitons and closer to the bow shock than the rest of the phenomena.

Figure 14b shows the distributions of the angles θ_{BN} of the portion of the model bow shock which different phenomena were magnetically connected to. These angles were calculated by obtaining the bow shock shape and size following the work of Greenstadt et al. (1972). The vast majority of angles for SHFAs and foreshock cavitons are smaller than 50° , as expected. There are a few outliers. A possible explanation for these events is that they occurred inside the traveling foreshocks so that the IMF vector, needed to calculate the θ_{BN} , was obtained upstream of these foreshocks.

Foreshock cavities show a broad distribution of θ_{BN} peaking between 40° and 60° , while a more flat distribution is seen in case of FCBs.

Figure 14c shows the distance (along the IMF direction) of the events to the model bow shock. Most events were observed at distances $\leq 12 R_E$, although this may partially be due to the fact that they were all observed by the Cluster spacecraft, which, when located upstream of the Earth's bow shock, tend to stay close to it.

SHFAs were all observed at distances $\leq 6 R_E$, which is expected, since they are supposed to form due to cavitons interacting with the bow shock. The distances of several R_E could be partially explained by the fact that SHFAs have finite sizes (the sizes of SHFAs may be similar to those of foreshock cavitons, which, as has been shown by Kajdič et al., 2013, are in rare cases more than $8 R_E$). Another point is that these distances are

along the IMF direction so SHFAs can actually be located upstream of a portion of the bow shock to which they do not seem to be magnetically connected but is closer to them.

Foreshock cavitons were also mostly observed at distances $\leq 5 R_E$ which is also expected since they are found in the regions containing compressive ULF waves. The distribution of distances of foreshock cavities peaks between $\sim 3 R_E$ and $\sim 5 R_E$, while that of FCBs is relatively flat between $0 R_E$ and $7 R_E$.

We put all known phenomena in context in Figure 15. This figure illustrates different boundaries, regions, and structures that populate them. They correspond to the observed phenomena shown in Figure 14a. The magnetic field line that barely touches the bow shock is called the tangential IMF line. Just downstream of it the spacecraft would first detect reflected electrons, so this region is called the electron foreshock (green). Farther downstream, where magnetic field lines connect to the quasi-parallel bow shock, begins the ion foreshock (yellow). There are no ULF waves in this region, and the reflected ions follow IMF lines, so they are called field-aligned ion beams (FABs). Still farther downstream, transverse ULF waves are also observed and this is where the ULF wave foreshock begins (purple). This region is delimited by a thick dash-dotted line that corresponds to the ULF wave boundary (Greenstadt & Baum, 1986) also shown in Figure 14a. In this region observed ion distributions change from FAB to intermediate. The thick dashed line corresponds to intermediate ion boundary (see Figure 14a and Meziane & d'Uston, 1998). Finally, a spacecraft crosses an FCB (thick dotted line) and enters the region (blue) with compressive ULF waves, shocklets, SLAMS, diffuse suprathermal ions, and other transient structures such as foreshock cavitons and SHFAs.

Another way to compare different phenomena is to look at the IMF and SW conditions under which they are observed. Figure 16a shows distributions of (from left to right) IMF magnitude, SW density, SW velocity, and SW thermal pressure for (from top to bottom) SHFAs, foreshock cavitons, foreshock cavities, and FCBs. Figure 16b is in the same format, but it shows distributions of (from left to right) SW temperature, IMF cone angle θ_{BX} , SW Alfvén velocity V_A , and Alfvénic Mach number M_A . No SHFAs were observed for $M_A < 6$ and $V_A > 90 \text{ km s}^{-1}$, although a larger sample should be analyzed to reach any definite conclusions. Distributions of SW and IMF

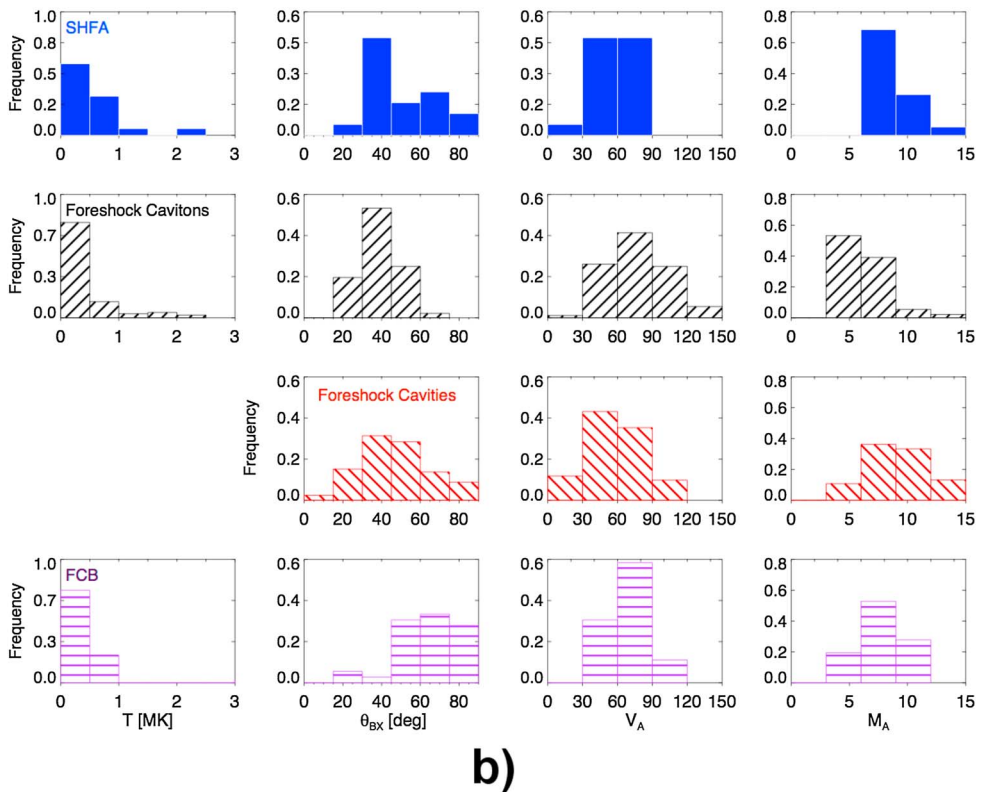
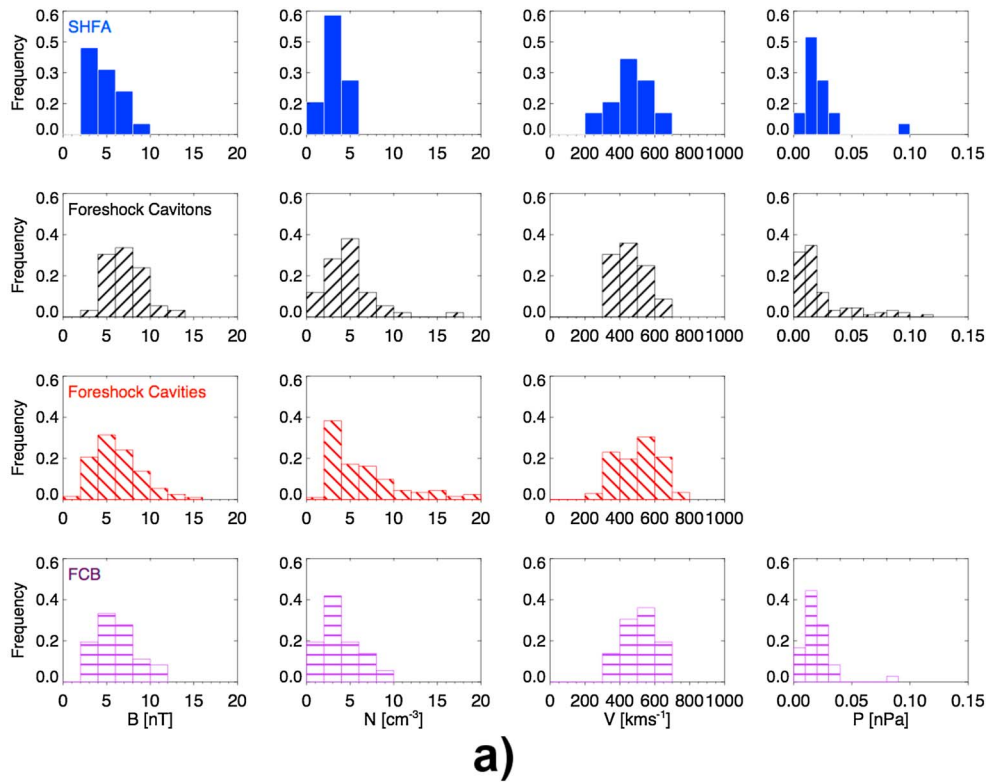


Figure 16. (a) Distributions of (from left to right) IMF magnitude, SW density, SW velocity, and SW thermal pressure for times when (from top to bottom) SHFAs, foreshock cavitons, foreshock cavities, and FCBs were observed. (b) The same as Figure 16a, but the distributions of the (from left to right) SW temperature, IMF cone angle θ_{Bx} , SW Alfvén velocity V_A , and Alfvénic Mach number M_A are shown.

properties in the case of cavities, cavitons, and FCBs are much more similar, although the ranges of B magnitude, plasma densities tend to be larger for cavities and cavitons. Although the distributions presented in this figure are subject to the intrinsic distributions of the IMF and SW properties, we can see that all four types of upstream transient structures may be observed under a wide range of SW and IMF conditions.

3. Discussion

In the first part of this paper we use multispacecraft data from the Cluster and THEMIS missions to confirm some predictions from Omidi et al. (2013a) hybrid simulations, namely, the existence of a traveling foreshock and the relation between some of the phenomena that are commonly observed upstream of the Earth's bow shock.

We postulate here that two types of foreshock may exist upstream of the Earth's bow shock: one is a global Earth's foreshock that forms upstream of a quasi-parallel section of the Earth's bow shock. It was shown by Omidi et al. (2013a) that during steady solar wind and IMF conditions a foreshock compressional boundary forms at the edge of a foreshock, delimiting a region of either pristine solar wind or a region of field-aligned ion beams from a region of diffuse ions that is populated by compressive ULF waves. In practice, the SW and the IMF are never exactly steady. IMF rotations are commonly observed in the solar wind (e.g., Borovsky, 2008). Such rotations may be slow, lasting for several minutes (as in our case study 1), or they can occur on very short times (approximately seconds). The latter are called rotational discontinuities. When two consecutive IMF rotations pass the Earth's bow shock, the foreshock changes its position with respect to the bow shock and may undergo back and forth motion. This can cause a spacecraft to enter the foreshock for a time period that can range from a few minutes to some tens of minutes and then exit it.

Foreshock observations on similar time scales can also occur when bundles of magnetic field lines with orientations different from the rest of the IMF sweep along the bow shock surface. In these cases a spacecraft located upstream of the shock observes two consecutive IMF RDs. The rotation of the IMF across such two RDs may be sufficient to temporarily change the geometry of a portion of the bow shock from quasi-perpendicular to quasi-parallel. The region of space between the two RDs becomes populated by suprathermal ions and compressive ULF fluctuations and resembles a global foreshock. However, because the RDs are convected by the SW antisunward, their intersection with the bow shock propagates along the bow shock surface in the direction roughly perpendicular to Sun-Earth line. The foreshock-like region between the RDs then also propagates in the same direction; hence, we call it a traveling foreshock.

Foreshock compressional boundaries form at the edges of both types of foreshock when they are observed under unsteady IMF conditions. FCBs are observed in the B and N profiles simultaneously either with slow rotations of the IMF or with IMF RDs. IMF rotation across FCBs has been analyzed by Rojas-Castillo et al. (2013). In their statistical study of FCBs these authors reported that the IMF cone angle changed by up to 15° across 36% of their events, while it changed between 15° and 30° across 42% of the events. However, Rojas-Castillo et al. (2013) did not look at whether or not all their FCBs were related to IMF slow rotations and IMF RDs. According to numerical simulations of Omidi et al. (2013a), B field rotations across FCBs occur even under steady IMF.

We further point out that other transient structures, isolated foreshock cavities, also form due to two successive IMF RDs. However, in the case of isolated cavities the two RDs are very closely separated, so the ULF waves are either not observed in the region between them or they are few. We conclude that these cavities are a subset of traveling foreshocks. The appearance of traveling foreshocks varies as the separation between the bounding IMF RDs increases. As the separation increases, the ULF waves begin to appear in the region between them. We illustrate this by showing a case study where only about 10 ULF waveforms are observed during the time between two IMF RDs.

The rotations of IMF can be easily understood if one imagines the IMF to be composed of magnetic flux tubes that extend from the solar surface into the interplanetary space. Borovsky (2008) performed a statistical study of flux tubes properties. These authors studied IMF rotations at 1 AU from 1998 to 2004 and concluded that small rotations with characteristic rotation angles of 15° occur due to IMF turbulence, while larger rotations occur when different magnetic flux tubes are convected across the observer. Borovsky (2008) estimated that the thicknesses of these flux tubes at heliocentric distance of 1 AU range from less than $10 R_E$ to several thousands of R_E with median sizes being $98 R_E$ and $67 R_E$ for the slow and fast solar wind, respectively.

These flux tubes exhibit very different durations in the spacecraft data. It is also suggested in the sketch in Figure 1 of Borovsky (2008) that the flux tubes neither are straight nor are they simply aligned along the Parker spiral but that they change their orientation in space. They can be distorted with wiggles, and they are interlaced. It is thus appropriate to suggest that slow IMF rotations, such as the one observed in our case study 1 (the global foreshock), occur when a large flux tube with a wiggle is being convected past the observer. We illustrate this idea in Figure 4c where a large magnetic flux tube is colored in red. The sketched flux tube exhibits a kink and is convected antisunward (downward in the figure) by the solar wind. As the kink passes the bow shock, the latter remains inside this flux tube but the orientation of the B field changes with time. In this case the spacecraft detect back and forth motion of the foreshock due to varying angle θ_{BN} .

Fast rotations and RDs (related to traveling foreshocks) on the other hand are observed as different flux tubes convect across the observer. We show such a situation in Figure 8b where the bow shock is initially inside the large kinked flux tube (red). At some point either the whole bow shock or just a portion of its surface briefly exits the red flux tube and enters a thinner flux one (blue) with different IMF orientation. In this case, multiple spacecraft detect the convecting foreshock signature.

We should note here that in case of very parallel IMF, the related RDs would also appear slow rotations since it would take a long time for a spacecraft to cross from one flux tube to another.

We also look at phenomena inside the traveling foreshock. We observe compressive ULF waves and in one case a spontaneous hot flow anomaly. This means that other structures may also form inside such foreshocks: compressive ULF waves may evolve into short-large-amplitude magnetic structures (SLAMS) (e.g., Thomsen et al., 1990; Schwartz & Burgess, 1991; Schwartz et al., 1992; Mann et al., 1994; Lucek et al., 2002) which may cause cyclic reformation of a portion of the Earth's bow shock. The interaction of compressive and transverse ULF waves leads to the formation of foreshock cavitons (Omidi, 2007), and interactions of cavitons with the bow shock lead to formation of the SHFAs (Zhang et al., 2013; Omidi et al., 2013b) and further to the rippling of the bow shock's surface. On the other hand, hybrid simulations suggest that foreshock cavitons and SHFAs may temporarily and locally weaken the bow shock, so its transition exhibits smaller B field magnitudes and densities (Blanco-Cano et al., manuscript in preparation).

Rippling and weakening of the bow shock may have consequences in the magnetosheath. Specifically, these processes have been identified as formation mechanisms for magnetosheath jets (e.g., Hietala et al., 2009). Jets have mostly been detected downstream of the quasi-parallel bow shock. IMF RDs are associated with traveling foreshocks, so the magnetosheath jets could sometimes appear in association with them.

In the second part of this paper we statistically compare observational properties of four foreshock phenomena (foreshock cavities, foreshock cavitons, foreshock compressional boundaries, and spontaneous hot flow anomalies), their observed locations, and the SW and IMF conditions under which they were detected. All of these phenomena show changes in the B field magnitude and plasma density when compared to the conditions of the ambient medium. All but FCBs show depletions of these two quantities in their centers. We show that SHFAs are the most depleted structures inside which the B field and N diminish typically by $\sim 90\%$. In the case of cavities and cavitons this number is between 40% and 50% on average. The changes in magnetic field and in density are most correlated in the case of foreshock cavitons and FCBs with correlation coefficients of 0.85 and 0.86, respectively. Strong depletions in the case of SHFAs are expected following the proposed explanation for their formation, namely, that they occur due to interactions of already depleted structures in the foreshock, the foreshock cavitons, with the bow shock. When this interaction occurs, the ions at their centers energize due to ion trapping by the cavitons and ion reflection between the bow shock and the cavitons and this leads to further depletion of B and N inside them (Zhang et al., 2013; Omidi et al., 2013b).

By comparing locations of the four phenomena in solar foreshock coordinates, we show that FCBs and foreshock cavities (or traveling foreshocks) occupy the same domain, which strengthens the proposal first made by Omidi et al. (2013a) that the two phenomena are related, namely, that FCBs occur at the cavities's edges. It should be pointed out here that the FCBs that occur at the edges of the global foreshock would also occupy the same domain. In SFC the FCBs and foreshock cavities are the phenomena that appear upstream of ULF waves, intermediate ion boundaries (related to global foreshock), while foreshock cavitons appear downstream of them. This makes sense since foreshock cavitons are the result of the interaction of transverse and compressive waves ULF waves and the compressive ULF wave appear further inside the foreshock than the ULF wave boundary studied by Greenstadt and Baum (1986). On the other hand, the FCBs and traveling foreshocks

are bounded by pristine solar wind which will position them upstream of all the other phenomena in the SFC coordinates.

Finally, we show that all four phenomena occur for a wide range of SW and IMF conditions.

4. Conclusions

Here we summarize the conclusions of this investigation:

1. There are two different types of foreshock detected upstream of the Earth's bow shock. One is the global foreshock located upstream of quasi-parallel section of the bow shock. This foreshock may change its location due to IMF rotations. Two successive IMF rotations may cause the back and forth motion of the foreshock resulting in brief excursions of the spacecraft into it that can last between several tens of minutes to several hours. Another type is the traveling foreshock which exists between two IMF RDs. This kind of foreshock usually lasts of the order of 10 min in the spacecraft data. We call it a traveling foreshock since it propagates along the bow shock surface. We should stress out though that when the flux tube is large enough, it can affect the whole bow shock surface so the resulting traveling foreshock will also be "global."
2. The difference between what is traditionally called the global foreshock and the traveling foreshock is not their size. In the case of back and forth motion of the global foreshock, the orientation of the IMF changes, but the bow shock remains inside the same flux tube. In case of traveling foreshock the bow shock (or a portion of it) magnetically connects to different flux tubes.
3. Foreshock compressional boundaries are observed at the edges of either type of foreshock.
4. Foreshock cavities are a subset of traveling foreshocks, where the two IMF RDs are so close that ULF waves are either not observed or only few of them are observed between the RDs. All the isolated foreshock cavities in the literature exhibit durations of less than 200 s in the data, while the traveling foreshocks can last for 10 or more minutes. We must, however, permit the possibility that on rare occasions the signatures in the spacecraft data very similar to those of foreshock cavities could also be observed due to the spacecraft brief encounters with the global foreshock.
5. Compressive ULF waves and transient foreshock structures inside traveling foreshocks can cause bow shock reformation and rippling. In the past shock rippling has been proposed as a formation mechanism for magnetosheath jets. These should then also appear in association with traveling foreshocks.
6. Foreshock transient structures, such as spontaneous hot flow anomalies, have been shown to exist inside the traveling foreshocks. According to present knowledge, the SHFAs are a product of foreshock cavities interacting with the Earth's bow shock. Hence, it should in principle be possible to observe foreshock cavities inside traveling foreshocks.
7. SHFAs are the most depleted structures in terms of B field and plasma density inside their cores when compared to the surrounding medium.
8. The changes in plasma density and B field are most correlated in case of FCBs and foreshock cavities.
9. The FCBs and foreshock cavities occupy the same domain in SFCs, which agrees with the idea that the FCBs form at the edges of the cavities (or traveling foreshocks).
10. Foreshock cavities, cavities, FCBs, and SHFAs can be observed under a wide range of SW and IMF conditions.

Some challenges remain for future work. Foreshock cavities have not yet been observed inside traveling foreshocks. We only find SHFAs inside these foreshocks and infer that cavities must also exist there. Similarly, we found compressive ULF waves but did not look for shocklets and SLAMS inside traveling foreshocks. Finally, simultaneous observations of traveling foreshock and magnetosheath jets would provide a conclusive piece of evidence of their possible relation.

References

- Auster, H. U., Glassmeier, K. H., Magnes, W., Aydogar, O., Baumjohann, W., Constantinescu, D., ... Wiedemann, M. (2008). The THEMIS fluxgate magnetometer. *Space Science Reviews*, 141(1), 235–264. <https://doi.org/10.1007/s11214-008-9365-9>
- Balogh, A., Carr, C. M., Acuna, M. H., Dunlop, M. W., Beek, T. J., Brown, P., ... Schwingenschuh, K. (2001). The Cluster magnetic field investigation: Overview of in-flight performance and initial results. *Annales de Geophysique*, 19, 1207–1217. <https://doi.org/10.5194/angeo-19-1207-2001>
- Billingham, L., Schwartz, S. J., & Sibeck, D. G. (2008). The statistics of foreshock cavities: Results of a Cluster survey. *Annales de Geophysique*, 26, 3653–3667. [Available at www.ann-geophys.net/26/3653/2008/]
- Billingham, L., Schwartz, S. J., & Wilber, M. (2011). Foreshock cavities and internal foreshock boundaries. *Planetary and Space Science*, 59(7), 456–467.

Acknowledgments

The authors are grateful to S.J. Schwartz for providing the processed observational data for foreshock cavities and to the Cluster Science Archive teams and the CL/CLWeb team for the easy access to the Cluster and THEMIS data. The data used in this work can be accessed on the corresponding Web pages: <http://clweb.irap.omp.eu> and <https://www.cosmos.esa.int/web/csa>. This work has been supported by the International Space Science Institute (ISSI). P.K.'s work was also supported by the DGAPA PAPIIT grant IA104416. X.B.C. and P.K. work was supported by DGAPA/PAPIIT grant IN105014 and CONACYT grant 179588. Work at GSFC was supported by the THEMIS mission; aastex-help@asas.org. Facilities: CSA.

- Blanco-Cano, X., Omidi, N., & Russell, C. T. (2009). Global hybrid simulations: Foreshock waves and cavitons under radial IMF geometry. *Journal of Geophysical Research*, *114*, A01216. <https://doi.org/10.1029/2008JA013406>
- Blanco-Cano, X., Kajdič, P., Omidi, N., & Russell, C. T. (2011). Foreshock cavitons for different interplanetary magnetic field geometries: Simulations and observations. *Journal of Geophysical Research*, *116*, A09101. <https://doi.org/10.1029/2010JA016413>
- Borovsky, J. E. (2008). Flux tube texture of the solar wind: Strands of the magnetic carpet at 1 AU?. *Journal of Geophysical Research*, *113*, A08110. <https://doi.org/10.1029/2007JA012684>
- Burgess, D., Lucek, E. A., Scholer, M., Bale, S. D., Balikhin, M. A., Balogh, A., ... Walker, S. N. (2005). Quasi-parallel shock structure and processes. *Space Science Reviews*, *118*, 205. <https://doi.org/10.1007/s11214-005-3832-3>
- Dorfman, S., Hietala, H., Astfalk, P., & Angelopoulos, V. (2017). Growth rate measurement of ULF waves in the ion foreshock. *Geophysical Research Letters*, *44*, 2120–2128. <https://doi.org/10.1002/2017GL072692>
- Eastwood, J. P., Lucek, E. A., Mazelle, C., Meziane, K., Narita, Y., Pickett, J., & Treumann, R. A. (2005). The foreshock. *Space Science Reviews*, *118*(1-4), 41–94. <https://doi.org/10.1007/s11214-005-3824-3>
- Fairfield, D. H. (1971). Average and unusual locations of the Earth's magnetopause and bow shock. *Journal of Geophysical Research*, *76*(28), 6700–6716. <https://doi.org/10.1029/JA076i028p06700>
- Fuselier, S. A., Thomsen, M. F., Gosling, J. T., & Bame, S. J. (1986). Gyrating and intermediate ion distributions upstream from the Earth's bow shock. *Journal of Geophysical Research*, *91*, 91–99.
- Gary, S. P. (1993). *Theory of Space Plasma Microinstabilities*. New York: Cambridge University Press.
- Gosling, J. T., Asbridge, J. R., Bame, S. J., Paschmann, G., & Sckopke, N. (1978). Observations of two distinct populations of bow shock ions in the upstream solar wind. *Geophysical Research Letters*, *5*, 957–960. <https://doi.org/10.1029/GL005i011p00957>
- Gosling, J. T., Asbridge, J. R., Bame, S. J., Paschmann, G., & Sckopke, N. (1979). Ion acceleration at the Earth's bow shock—A review of observations in the upstream region. *Geophysical Research Letters*, *5*, 957.
- Greenstadt, E. W. (1972). Binary index for assessing local bow shock obliquity. *Journal of Geophysical Research*, *77*(28), 5467–5479. <https://doi.org/10.1029/JA077i028p05467>
- Greenstadt, E. W., & Baum, L. W. (1986). Earth's compressional foreshock boundary revisited: Observations by the ISEE 1 magnetometer. *Journal of Geophysical Research*, *91*, 9001–9006.
- Hada, T., & Kennel, C. F. (1987). Excitation of compressional waves and the formation of shocklets in the Earth's foreshock. *Journal of Geophysical Research*, *92*(A5), 4423–4435.
- Hietala, H., Laitinen, T. V., Andréevová, K., Vainio, R., Vaivads, A., Palmroth, M., ... Rème, H. (2009). Supermagnetosonic jets behind a collisionless quasiparallel shock. *Physical Review Letters*, *103*, 245001.
- Hoppe, M. M., & Russell, C. T. (1981). On the nature of ULF waves upstream of planetary bow shocks. *Advances in Space Research*, *1*, 327–332.
- Hoppe, M. M., & Russell, C. T. (1983). Plasma rest frame frequencies and polarizations of the low-frequency upstream waves' ISEE 1 and 2 observations. *Journal of Geophysical Research*, *88*(A3), 2021–2028.
- Jelinek, K., Němeček, Z., & Šafránková, J. (2012). A new approach to magnetopause and bow shock modeling based on automated region identification. *Journal of Geophysical Research*, *117*, A05208. <https://doi.org/10.1029/2011JA017252>
- Kajdič, P., Blanco-Cano, X., Omidi, N., & Russell, C. T. (2011). Multi-spacecraft study of foreshock cavitons upstream of the quasiparallel bow shock. *Planetary and Space Science*, *59*, 705–714.
- Kajdič, P., Blanco-Cano, X., Omidi, N., Meziane, K., Russell, C. T., Sauvaud, J.-A., ... Lavraud, B. (2013). Statistical study of foreshock cavitons. *Annales de Geophysique*, *31*, 2163–2178. <https://doi.org/10.5194/angeo-31-2163-2013>
- Kis, A., Scholer, M., Klecker, B., Möbius, E., Lucek, E. A., Rème, H., ... Kucharek, H. (2004). Multi-spacecraft observations of diffuse ions upstream of Earth's bow shock. *Journal of Geophysical Research*, *31*, L20801. <https://doi.org/10.1029/2004GL020759>
- Kis, A., Scholer, M., Klecker, B., Kucharek, H., Lucek, E. A., & Rème, H. (2007). Scattering of field-aligned beam ions upstream of Earth's bow shock. *Annales de Geophysique*, *25*, 785. <https://doi.org/10.5194/angeo-25-785-2007>
- Lucek, E. A., Horbury, T. S., Dunlop, M. W., Cargill, P. J., Schwartz, S. J., Balogh, A., ... Georgescu, E. (2002). Cluster magnetic field observations at a quasi-parallel bow shock. *Annales de Geophysique*, *20*, 1699–1710.
- Mann, G., Lühr, H., & Baumjohann, W. (1994). Statistical analysis of short large-amplitude magnetic field structures in the vicinity of the quasi-parallel bow shock. *Journal of Geophysical Research*, *99*, 13,315–13,323.
- McFadden, J. P., Carlson, C. W., Larson, D., Angelopoulos, V., Ludlam, M., Abiad, R., ... Marckwordt, M. (2008). The THEMIS ESA plasma instrument and in-flight calibration. *Space Science Reviews*, *141*, 277–302. <https://doi.org/10.1007/s11214-008-9440-2>
- Meziane, K., & d'Uston, C. (1998). A statistical study of the upstream intermediate ion boundary in the Earth's foreshock. *Annales de Geophysique*, *16*, 125–133. <https://doi.org/10.1007/s00585-998-0125-7>
- Meziane, K., Hamza, A. M., Wilber, M., Mazelle, C., & Lee, M. A. (2013). On the field-aligned beam thermal energy. *Journal of Geophysical Research: Space Physics*, *118*, 6946–6954. <https://doi.org/10.1002/2013JA019060>
- Meziane, K., Alrefay, T. Y., & Hamza, A. M. (2014). On the shape and motion of the Earth's bow shock. *Planetary and Space Science*, *93-94*, 1–9. <https://doi.org/10.1016/j.pss.2014.01.006>
- Omidi, N. (2007). Formation of cavities in the foreshock, *Turbulence and Nonlinear Processes in Astrophysical Plasmas: 6th Annual International Astrophysics Conference* (Vol. 932, pp. 181–190). Solana Beach, Calif.: AIP Conference Proceedings. <https://doi.org/10.1063/1.2778962>
- Omidi, N., Sibeck, D., & Blanco-Cano, X. (2009). The foreshock compressional boundary. *Journal of Geophysical Research*, *114*, A08205. <https://doi.org/10.1029/2008JA013950>
- Omidi, N., Sibeck, D., Blanco-Cano, X., Rojas-Castillo, D., Turner, D., Zhang, H., & Kajdič, P. (2013a). Dynamics of the foreshock compressional boundary and its connection to foreshock cavities. *Journal of Geophysical Research: Space Physics*, *118*, 823–831. <https://doi.org/10.1002/jgra.50146>
- Omidi, N., Zhang, H., Sibeck, D., & Turner, D. (2013b). Spontaneous hot flow anomalies at quasi-parallel shocks: 2. Hybrid simulations. *Journal of Geophysical Research: Space Physics*, *118*, 173–180. <https://doi.org/10.1029/2012JA018099>
- Omidi, N., Zhang, H., Chu, C., Sibeck, D., & Turner, D. (2014). Parametric dependencies of spontaneous hot flow anomalies. *Journal of Geophysical Research: Space Physics*, *119*, 9823–9833. <https://doi.org/10.1002/2014JA020382>
- Paschmann, G., Sckopke, N., Bame, S. J., Gosling, J. T., Russell, C. T., & Greenstadt, E. W. (1979). Association of low-frequency waves with suprathermal ions in the upstream solar wind. *Geophysical Research Letters*, *6*, 209–212.
- Pfau-Kempff, Y., Hietala, H., Milan, S. E., Juusola, L., Hoilijoki, S., Ganse, U., ... Palmroth, M. (2016). Evidence for transient, local ion foreshocks caused by dayside magnetopause reconnection. *Annales de Geophysique*, *34*, 943–959. <https://doi.org/10.5194/angeo-34-943-2016>
- Rème, H., Aoustin, C., Bosqued, J. M., Dandouras, I., Lavraud, B., Sauvaud, J. A., ... Sonnerup, B. (2001). First multispacecraft ion measurements in and near the Earth's magnetosphere with the identical Cluster Ion Spectrometry (CIS) experiment. *Annales de Geophysique*, *19*, 1303–1354. <https://doi.org/10.5194/angeo-19-1303-2001>

- Rojas-Castillo, D., Blanco-Cano, X., Kajdič, P., & Omid, N. (2013). Foreshock compressional boundaries observed by Cluster. *Journal of Geophysical Research: Space Physics*, 118, 698–715. <https://doi.org/10.1029/2011JA017385>
- Schwartz, S. J., & Burgess, D. (1991). Quasi-parallel shocks: A patchwork of three-dimensional structures. *Geophysical Research Letters*, 18, 373–376. <https://doi.org/10.1029/91GL00138>
- Schwartz, S. J., Burgess, D., Wilkinson, W. P., Kessel, R. L., Dunlop, M., & Lühr, H. (1992). Observations of short large-amplitude magnetic structures at a quasi-parallel shock. *Journal of Geophysical Research*, 97, 4209–4227. <https://doi.org/10.1029/91JA02581>
- Sibeck, D. G., Phan, T.-D., Lin, R., Lepping, R. P., & Szabo, A. (2002). Wind observations of foreshock cavities: A case study. *Journal of Geophysical Research*, 107(A10), 1271. <https://doi.org/10.1029/2001JA007539>
- Schwartz, S. J., Sibeck, D., Wilber, M., Meziane, K., & Horbury, T. S. (2006). Kinetic aspects of foreshock cavities. *Geophysical Research Letters*, 33, L12103. <https://doi.org/10.1029/2005GL025612>
- Thomsen, M. F. (1985). Upstream suprathermal ions. In B. T. Tsurutani, & R. G. Stone (Eds.), *Collisionless Shocks in the Heliosphere: Reviews of Current Research* (pp. 253–270). Washington, DC: AGU. <https://doi.org/10.1029/GM035p0253>
- Thomsen, M. F., Gosling, J. T., Bame, S. J., & Russell, C. T. (1990). Magnetic pulsations at the quasi-parallel shock. *Journal of Geophysical Research*, 95, 957–966.
- Treuman, R. A. (2009). Fundamentals of collisionless shocks for astrophysical application: 1. Non-relativistic shocks. *Astronomy and Astrophysics Review*, 17, 409–535. <https://doi.org/10.1007/s00159-009-0024-2>
- Winterhalter, D., & Kivelson, M. G. (1988). Observations of the Earth's bow shock under high Mach number/high plasma beta solar wind conditions. *Geophysical Research Letters*, 15(10), 1161–1164. <https://doi.org/10.1029/GL015i010p01161>
- Zhang, H., Sibeck, D. G., Zong, Q.-G., Omid, N., Turner, D., & Clausen, L. B. N. (2013). Spontaneous hot flow anomalies at quasi-parallel shocks: 1. Observations. *Journal of Geophysical Research: Space Physics*, 118, 3357–3363. <https://doi.org/10.1002/jgra.50376>